Additive Manufacturing 81 (2024) 103977

Contents lists available at ScienceDirect

Additive Manufacturing

journal homepage: www.elsevier.com/locate/addma

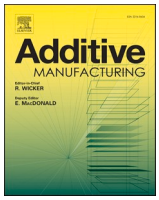

4D printing of poly-Pickering high internal phase emulsions to assembly a thermo-responsive shape-memory hierarchical macroporous scaffold

Mahdiyar Shahbazi [a,*,1], Henry Jäger [a,*], Rammile Ettelaie [b], Jianshe Chen [c], Adeleh Mohammadi [d], Peyman Asghartabar Kashi [e]

[a] Institute of Food Technology, University of Natural Resources and Life Sciences (BOKU), Muthgasse 18, 1190, Vienna, Austria
[b] Food Colloids and Bioprocessing Group, School of Food Science and Nutrition, University of Leeds, Leeds LS2 9JT, UK
[c] Food Oral Processing Laboratory, School of Food Science & Biotechnology, Zhejiang Gongshang University, Hangzhou 310018, China
[d] Faculty of Food Science and Technology, Gorgan University of Agricultural Sciences and Natural Resources, Gorgan 4913815739, Iran
[e] Faculty of Biosystem, College of Agricultural and Natural Resources, Tehran University, 31587–77871 Karaj, Iran

ARTICLE INFO

Keywords:
Thermo-responsive polymers
4D printing
Cellulose nanocrystals
Poly-HIPEs
Droplet flocculation
Macroporous scaffold
Shape-memory effect

ABSTRACT

Because of their enormous potential in biofabrication, adsorption, catalysis, and energy conversion applications, there has been substantial attention to fabricating 4D printed hierarchically porous structures from the molecular level to the macroscopic dimensions. To this end, an understanding of the structure-feature relationship of smart materials in 4D printing is necessary to design innovative constructs, which are not limited to any specific degree of freedom. Here, we report on the fabrication of thermo-responsive macroporous polymerized-high internal phase emulsions (poly-HIPEs) through 3D printing of Pickering-type HIPEs. The oil-in-water Pickering-HIPE-based inks contained methylcellulose/kappa-carrageenan blend (non-crosslinked) as a continuous phase, which was colloidally stabilized by a hybrid of cellulose nanocrystals and cellulose nanofibers. The Pickering-HIPE-based inks showed a non-linear and time-dependent oscillatory response with excellent viscoelastic interfacial properties. The poly-Pickering-HIPEs were readily fabricated by *in-situ* crosslinking of Pickering-HIPEs during hot-melt extrusion-based printing, which produced a series of 3D printed thermo-responsive hierarchical macroporous structures. The 4D printed objects presented a highly interconnected open-cell porous structure, which was thermo-responsive in nature. Moreover, these 4D structures showed high mechanical strength with outstanding self-recovery performance. Our results offer the prospect of developing a thermo-responsive macroporous construct having shape memory features at different temperatures by regulating emulsion formulation.

1. Introduction

The fabrication of next-generation engineering scaffolds with improved multifunctionality needs the rational designs of structured materials, supported by an understanding of basic structure–function relations. Engineering of these hierarchically porous structures over diverse dimensions imitates biological building blocks, which provide an assortment of multifunctionalities required for different applications. There has been an increasing interest in using such biocompatible and bioactive structures having hierarchical macroporous matrices in different applications, such as semiconductors [1], energy conversion and storage [2], food applications [3], biofabrication [4], catalysis [5], vascular stents [6], drug delivery [7], bone substitute materials [8], and pollution abatement [9]. The hierarchically porous structures show a property ranging from micropores (<2 nm), and mesopores (2–50 nm) to macropores (>50 nm), determining how the scaffolds meet contradictory physicomechanical properties and mass transport requirements. To fabricate a well-defined hierarchically macroporous structure, bottom-up methods related to the self-assembly routes can be also employed [10–13].

The adaptability of the processing techniques along with controlling the pore diameters can be important challenges and remain the subjects of ongoing research studies. Thus, designing and engineering effective and eco-friendly approaches to construct hierarchically porous structures are crucial for their biocompatibility and environmental stability. In recent years, 3D printing techniques have been utilized to

* Correspondence to: University of Natural Resources and Life Sciences (BOKU), Muthgasse 18, 1190 Vienna, Austria.
E-mail addresses: mahdiyar.shahbazi@boku.ac.at, shahbazim00@yahoo.com (M. Shahbazi), henry.jaeger@boku.ac.at (H. Jäger).
[1] Orcid https://orcid.org/0000–0002-2485–9130

https://doi.org/10.1016/j.addma.2024.103977
Received 31 July 2023; Received in revised form 26 November 2023; Accepted 7 January 2024
Available online 13 January 2024

manufacture functional complex 3D structures having hierarchically porous structures [14–18]. This technology holds great promise regarding custom-designed, cost-effective, high-value production, and rapidly prototyped 3D structure construction [7,19–25]. The fast-growing extrusion-based rapid prototyping method allows a potent means to construct a 3D object with controllable micro- and macro structures [26–29]. However, 3D printing of customized objects including non-functionalized biopolymers lacks critical mechanical properties and multifunctionalities [30–32]. Therefore, the integration of smart materials (such as thermo-responsive polymers) into 3D printing is an unavoidable method for the effective engineering of advanced soft systems through additive manufacturing [24,33]. For this reason, the Tibbits research group from the Massachusetts Institute of Technology (MIT) proposed the idea of 4D printing, which includes the application of a "space-time axis" concerning the 3D coordinate axis [33]. It is similar to the 3D printing process, but there is additional 3D design progress and printing of a smart polymeric-based structure using a 3D printing system. The 4D printing offers smart functional printing polymers, which alter their original shape upon exterior stimuli into products for various biomedical and bioengineering applications. This technique facilitates printed objects or parts larger than the printing systems themselves. Thus, 4D structures can unfold or shrink and constructs that are too large to fit in the printing system could be compressed for 3D printing.

To effectively control the hierarchical macroporous matrix, 4D printing can be ingeniously combined with more versatile printable inks to assemble a highly porous 3D structure. Different printable inks have been utilized to fabricate hierarchically macroporous structures, offering simple yet efficient control of the porous matrix using numerous formulation parameters. Reportedly, emulsion-templated approaches have been a promising technique to fabricate hierarchically porous structures [34]. Among them, high internal phase emulsions (HIPEs) (with a volume portion of internal phase greater than 0.74) have received great attention due to providing a well-defined structure and widespread applications in tissue engineering [35,36], absorption [37–40], food application [41], controllable drug release [42,43], and water purification [44–48].

Traditional HIPEs have been stabilized using molecular surfactants in a range of 5–50% [49]. Yet, HIPE stabilization shows a challenge in the development process of macroporous structures [50]. The particle-stabilized HIPEs, also known as Pickering-HIPEs, have been developed in the absence of any surfactants, in which the solid particles can be adsorbed at the O/W interfaces. Compared to traditional HIPEs, they are extremely stable due to the irreversible adhesion of solid particles at the O/W interface [50–52], utilization of less toxic materials [53], improvement of mechanical properties of macroporous polymers [54], and inducing some novel properties and functionally [55,56], for example, magnetic macroporous polymers [56]. It has been proved that cellulose-based nanomaterials, including cellulose nanofibers (CNFs) and cellulose nanocrystals (CNCs), can develop highly stable HIPEs either by synergy with surfactants or as unique emulsifying agents [57–59]. The application of diverse nanomaterials in hybrids produces innovative functional inks from a combined strengthening, making environmentally friendly, robust, and bio-based strategies for 4D printing applications. For example, it was reported that the combination of CNC and CNF has resulted in a synergistic stabilization of HIPEs [60]. It was concluded that the adsorption of CNC at the O/W interface allowed Pickering emulsions to be stabilized by intruding hybrid CNC and CNF, in which the micrometer droplet sizes of this emulsion experienced excellent depletion stabilization.

Recently, the polymerized Pickering-HIPEs (known as poly-Pickering-HIPEs) have been used as templates to prepare highly porous polymers with stimuli-responsive properties like thermo-responsive behavior [61–63]. Commonly, the poly-Pickering-HIPEs show a closed-cell structure, which was related to the physical stability of HIPEs (infrequent coalescence) with an inflexible barrier of solid nanoparticle layers at the interface. Methylcellulose (MC) and kappa-carrageenan (KC) are promising sustainable polymers utilized to develop thermo-responsive poly-Pickering-HIPE-based gels [63,64] with a temperature-dependents–gel transitions from 60 to 80 °C [65]. One of the factors that influence the critical solution temperature of MC and their mechanism of action is the grafting of the biomacromolecules. Some polymers like KC [66,67], acting like electrolytes, destabilize MC-water interactions and enhance the CH_3-CH_3 interactions between MC macromolecules. This results in a reduction of critical solution temperature in the MC-containing blend. With the different amounts of KC and MC from 1 to 2 wt%, a sol–gel transition was designed to happen in the physiologic range (30–60 °C), paving the way for entrapment and releasing therapeutic colloids [67].

Here, we report on the integration of poly-Pickering-type HIPEs-gel with 3D printing to develop a thermo-responsive shape-memory hierarchically macroporous scaffold. To this end, a 3D printable O/W Pickering-HIPEs based on the MC/KC blend (as a continuous phase) was initially prepared. This system was stabilized by a hybrid of CNC and CNF. Next, an *in-situ* crosslinking of Pickering-HIPEs was performed during 3D printing to develop thermo-responsive macroporous poly-Pickering-HIPEs. The preparation conditions to fabricate 3D printed poly-Pickering-HIPEs scaffolds were investigated by evaluation of rheological features, morphological characterization, and colloidal stability of Pickering-HIPEs. The shape recovery behavior, stimuli-response properties, microscopic pore structure, and mechanical strength of 3D printed poly-Pickering-HIPEs upon selective stimuli of heat were assessed based on their quantitative printing performance and shape memory properties.

2. Experimental section

2.1. Materials

Methylcellulose (MC) (Mw (g mol^{-1}) = 11 × 10^4; Mn (g mol^{-1}) = 44 × 10^3; viscosity = 0.2 Pa s; and DS = 1.6–1.7) was purchased from LOTTE Fine Chemical Co. Ltd (Incheon, Korea). Kappa-carrageenan (KC) (10–25 mPa s, 0.3%, water, 25 °C) was obtained from Tokyo Chemical Industries (Tokyo, Japan). Ultra-refined de-waxed sunflower oil (>98%, Vandermoortele NV, Breda, the Netherlands) possessed a dielectric constant of 2.9% and 98% triglycerides mean values of 70.2% and 25.1% for linoleic and oleic acids, respectively. Wood pulp CNF suspension (solid content of 1.0 wt%) and CNC were obtained from Shanghai ScienceK Nanotechnology Ltd. and Qihong Technology Co., Ltd., respectively. *N,N′*-methylene bisacrylamide (MBA) was provided by Macklin (Shanghai, China). All water was deionized which is generated by reverse osmosis (Ultra-Purified Type I, 18.2 Megohm water). Other reagents were commercial grade and used without further purification.

2.1.1. Preparation of Pickering-HIPE-based inks

To prepare the aqueous phase of O/W HIPEs, a blend of MC/KC was initially prepared as follows: The stock aqueous solution of MC was obtained by dissolving MC (4 wt%) in deionized water, which was vigorously stirred at 70 °C (according to differential scanning calorimetry or DSC of pure MC presented in section S.1 in Supplementary Materials) using a high-speed homogenizer (IKA T18 Ultra-Turrax, Staufen, Germany) for 120 min. The MC solution was then allowed to cool down gradually and stored at 4 °C overnight to be fully hydrated. Separately, a weighed amount of KC powder was dissolved in deionized water and vigorously stirred at 60 °C for 60 min to prepare a 2% (w/v) KC-based solution. Following this, a binary blend aqueous dispersion was prepared by mixing different mass ratios of MC/KC (0.0/1.0, 0.2/0.8, 0.4/0.6, 0.6/0.4, 0.8/0.2, and 1.0/0.0) and was kept at 4 °C before measurements. According to results of Fourier-transform infrared spectroscopy (FT-IR), DSC, and contact angle measurements (section S.1 in Supplementary Materials), the MC/KC with a ratio of 0.8/0.2 offered a

successful development of MC/KC blend system (Fig. S-1a in Supplementary Materials), providing an improved surface hydrophobicity (Fig. S-1b in Supplementary Materials) with excellent thermoresponsive behavior (Figs. S-1c,d in Supplementary Materials), which was suitable to produce the continuous phase of HIPEs.

To produce O/W Pickering-HIPEs (with a total volume of 60 mL), as-prepared MC/KC blend dispersion (15 mL) was mixed with the oil phase (45 mL) (*i.e.*, the oil phase volume fraction was 75%). To stabilize O/W HIPEs, the CNC and CNF were separately used in two consecutive methods to colloidally stabilize the HIPEs. First, the CNC at a fixed level of 1.5 wt% was incorporated into the MC/KC aqueous phase, which was optimized based on the colloidal stability measurement using a static multiple light scattering assay. This assay was conducted *via* Turbiscan LAB equipment (Formulaction, Toulouse, France), which was employed to assess the real-time stability of Pickering-HIPEs (Supplementary Materials, Section S.2). The CNC-included O/W HIPEs were initially emulsified through a high-shear rotor-stator device (SilentCrusher 130 M, Heidolph, Germany) operating at 12,000 rpm for 2 min, followed by the application of a high-intensity sonication process (VC 750, Sonics & Materials, Inc., CT) fitted with a 13 mm diameter probe. The high-intensity emulsification process was accomplished close to the top surface of the O/W mixture at a frequency of 20 kHz; an amplitude of 60%; and a power of 450 W, with an on/off cycle of 10 s/4 s.

In the next phase, CNF with six different concentrations (0.0–1.0 wt %) was chosen to assess its ability to further stabilize the CNC-included O/W HIPEs. In this case, the diverse levels of CNF suspensions (as produced by the dilution of the stock CNF suspension at a concentration of 2 wt%) were incorporated into the Pickering-HIPE-based inks that included CNC (1.5 wt%) (Supplementary Materials, Section S.2). The O/W Pickering-HIPEs were then homogenized by a sonication system (VC 750, Sonics & Materials, Inc., CT) at a frequency of 20 kHz for 5 min. The oil concentration in the final Pickering-HIPEs was 7.5 wt% while CNF levels were included to be 0.0, 0.2, 0.4, 0.6, 0.8, and 1.0 wt%. The CNC/CNF-stabilized Pickering-HIPEs were signed as PPH-2, PPH-4, PPH-6, PPH-8, and PPH-10, which proposed the emulsions containing 0.2, 0.4, 0.6, 0.8, and 1.0 wt% CNF, respectively. The control (PPH-0) was the Pickering-HIPEs with no added CNF (yet includes CNC at a fixed level of 1.5 wt%). It is noteworthy to note that we evaluated the possible effect of MC, KC, and a blend of MC/KC (with no CNC and CNF in the physical stabilization of HIPEs (Section S.3 in Supplementary Materials). Based on our results, we did not produce HIPEs with no CNC/CNF as the prepared emulsion system was physically unstable and was prone to a clear phase separation.

2.2. Characterization of Pickering-HIPEs-based ink

2.2.1. Emulsion stability by vertical laser profiling

The stability experiment was performed by vertical laser profiling using a Turbiscan Lab Expert stability analyzer (Formulaction, Toulouse, France) for 180 min under ambient conditions. The emulsion stability was carried out according to multiple light backscattering of a pulsed near-infrared light (880 nm). First, the emulsions were moved to a test bottle attaining a height of 48 mm and scanned the entire height of the inks every 4 h for 7 times, and the differences in the back-scattering and transmission light (*T*) were detected. The following formula was applied:

$$T \quad (l, r) = T_0 \exp(2r_i/l) \tag{1}$$

Here, r_i is the inner diameter of the sample cell and T_0 is the transmittance of the continuous phase (water).

From the physical point of view, the $l(d, \varphi)$ is calculated according to the following equation:

$$l \quad (d, \varphi) = (2d/3\varphi Q_s) \tag{2}$$

where d is the mean diameter of the droplets, φ the volume fraction of droplets, and Q_s is the optical parameter from Mie theory.

Moreover, the transmittance detector received the light that passed through the dispersion at an angle of 180° concerning the source, while the backscattering (*BS*) detector received the light scattered backward by the emulsion at an angle of 45°. The emulsion stability was determined with the *TSI* as follows:

$$TSI = \sum_{i=1}^{n} (x_i - x_{BS})^2 \Big/ n - 1 \tag{3}$$

where, λ * is the photon transport mean free path, φ is the particles' volume fraction, d is the particles' mean diameter, and g and Qs are the optical parameters assumed with the Mie theory. The χ_i is the average backscattering for each minute during the experiment, χ_{BS} is the average χ_i, and n is the number of scans.

2.2.2. Particle size measurement

The droplet sizes and particle size distribution of the inks were measured with a laser diffraction device (MS2000, Malvern Instruments Ltd., Worcestershire, UK), measuring the size based on the scattering of a monochromatic beam of laser light ($\lambda = 632.8$ nm). The droplet size was specified as the surface area mean diameter, $d_{(3,2)} = (\sum n_i d_i^{\,3} / \sum n_i d_i^{\,2})$, where n is the number of droplets with diameter d_i. The electrical charges (ζ-potential) of the printable inks were also obtained through a Zetasizer Nano-ZS90 (Malvern Instruments, Worcester-shire, UK) at a fixed detector angle of 90°.

2.2.3. Confocal laser scanning microscopy (CLSM)

The interfacial framework and network structure in the continuous phase of the Pickering-HIPEs were imaged *via* an FV-300 confocal laser scanning microscopy system (CLSM, Olympus, Tokyo, Japan) coupled with an Olympus IX71 inverted microscope and an argon-ion laser. The collected top emulsion layers were stained with a fluorescent dye before observation. The oil phase was dyed by adding 10 μL of Nile red solution (1 mg mL^{-1} ethanol) to 100 μL collected samples. After homogeneously mixing using a pipette, 6 μL of dyed samples was placed on a microscope slide (Assistent, Sondheim, Germany) and covered with a glass coverslip (18 mm × 18 mm, Assistent, Sondheim, Germany). The coverslip was quickly fixed with nail polish to avoid evaporation. The excitation and emission spectra for Nile red were 488 nm and 539 nm, respectively. All images were obtained at 40x magnification and processed using Olympus Fluoview software (version 2.1, Olympus, Tokyo, Japan).

2.2.4. Rheological experiment

The rheological behavior of ink samples was characterized by an AR 2000ex rheometer (TA Instruments, New Castle, DE) using a parallel plate geometry (diameter 40 mm, gap 1 mm). To evaluate the steady rheological properties, the shear stress (τ) was measured as a function of increasing shear rate ($\dot{\gamma}$) from 0.1–500 s^{-1}. The oscillatory strain sweep (0.1–200%, 1 Hz) was performed to attain the limitation of the linear viscoelastic region (*LVR*). Besides, the frequency sweep test (ω) (0.1–400 Hz) was accomplished in the *LVR* ($\gamma = 1\%$). All measurements were performed at 25 °C. The rheological parameters including elastic modulus (G') and loss modulus (G'') were evaluated by the manufacturer-supplied computer software (TRIOS, TA Instruments, West Sussex, UK).

Finally, a five-interval thixotropy test (5-ITT) was used to gather thixotropic data on the emulsions. This test was used to evaluate if the Pickering-HIPEs are prone to rapid recovery upon being sheared at the large deformations. Perfectly, a material can be shown as an ideal thixotropic structure if the peak viscosity in the third interval recovers at least 70% of its value measured after the initial interval. The 5-ITT detected the viscosity profiles of the samples under alternating high and low shear rates (100 and 0.1 s^{-1}, respectively) both for 100 s.

2.2.5. Quartz crystal microbalance with dissipation monitoring (QCM-D)

A QCM-D (Q-Sense E4 AB, Gothenburg, Sweden) was used to eval-

uate the adsorption properties of Pickering-HIPEs with the ability to detect variations of resonance frequency (Δf) and energy dissipation (ΔD) of QCM-D sensors. The gold sensors with a fundamental resonance frequency of 4.95 MHz (QSX 301) were cleaned and coated with a monolayer of sunflower oil by spin coating at 2000 rpm for 2 min with the oil solution (0.1 wt% in chloroform). The experiment was conducted at a flow rate of 50 μL min^{-1} at ambient conditions, and the Milli-Q water was used to establish a signal baseline. The Sauerbrey equation was used to make a relationship between Δf and the coupled mass (Δm):

$$\Delta m = -C(\Delta_f/n) \quad (4)$$

In the above equation, C is a mass constant depending on the physical property of the sensor (17.7 ng cm^{-2} Hz^{-1} for a 5 MHz crystal), and n is the resonance number of the sensor (n = 1, 3, 5, 9, 11, 13). For the sake of simplicity, only one harmonic ($n = 5$) was presented in the results here. In the current work, the fifth harmonic was employed to measure the dissipation shifts and frequency, as well as to obtain the corresponding mass change.

2.3. The 3D/4D printing of Pickering-HIPE-based inks

2.3.1. The 3D/4D printing process: Pickering-HIPEs to poly-Pickering-HIPEs

Before the printing process of ink, 100 μL of MBA solution (2 wt%), as a crosslinker, was mixed with 5.5 mL of Pickering-HIPEs. Immediately, the mixture was vigorously stirred at ambient conditions. Set the Pickering-HIPE-based inks at ambient temperature for 24 h. To evaluate the effect of crosslinker, a Pickering-HIPE (contained MC/KC with 0.08 wt% CNF and 1.5 wt% CNC) was also printed, but with no crosslinker (defined as PH-C). To fabricate 4D printed poly-Pickering-HIPEs, the prepared Pickering-HIPE-based inks were printed through an extrusion-based 3D printer (nScrypt-3D-450, nScrypt, Orlando, FL), which was connected to a syringe pump (PHD Ultra; Harvard Apparatus Holliston, MA). Different special 3D shapes (1D zigzag pattern, 2D square lattice, 3D DNA helix, butterfly, and a flower with 5 petals) were modeled by the application of computer-aided design software (AutoCAD; Autodesk Inc., San Rafael, CA), and converted to an STL file. The print paths were provided through the creation of the G-code files to control the XYZ direction instruction of the printer, developed by the open-source CAM software Slic3r from the STL file. The printable Pickering-HIPE-based inks were poured into a stainless-steel cartridge (10 mL) and stirred with a vortex mixer (Fisher Scientific, Ontario, Canada) for 15 min to remove the air bubbles from the ink. The Pickering-HIPEs were then printed through a needle diameter of 1 mm with an extrusion flow speed of 25 mL min^{-1} at 75 °C on a special plastic surface. After that, the resulting 4D printed constructs were alternately washed with absolute ethanol and deionized water to remove the internal phase, followed by freeze-drying (Martin Christ, Alpha 2–4 LD Plus, Osterode am Harz, Germany) to yield poly-Pickering-HIPEs.

2.3.2. Printing performance of 4D printed poly-Pickering-HIPEs

Each 3D printed object was transferred into a specific chamber (20 × 20 × 20) cm^3 for taking photos using a digital camera (Alpha 7M3 E-Mount, Full-Frame Mirrorless, 24.2 MP, Sony, Tokyo, Japan). The printing performance of 3D printed architectures was accomplished by determining through a digital caliper (Mitutoyo, Absolute Digimatic, Tokyo, Japan).

2.3.3. Microstructure evaluations of 4D structures

The morphological structure of the 4D printed objects was captured through a field-emission scanning electron microscope (FE-SEM, S-4700, Hitachi, Japan) to produce high-resolution images with a high depth of field. Initially, each 3D construct was cut into a precise size of (15 × 15 × 15) mm^3. Next, the sectioned 3D printed samples were mounted on a Peltier-cooled stage with a temperature of − 10 °C to avoid thermal damage. The nitrous oxide was utilized as an imaging gas that offered a pressure of 50.7 Pa. The microstructures of each 3D construct were obtained through a solid-state backscatter detector *via* an accelerating voltage of 20 kV.

Atomic force microscopy (AFM) assay was obtained by data collected in the tapping mode using a Nanoscope V Multimode scanning probe microscope (SPM, Veeco Instruments, Santa Barbara, CA). The peak force quantitative nanomechanical property mapping (QNM) was employed to obtain height images with a Cantilever C on conductive platinum-coated tips (HQ: NSC35/Pt, Mikromasch, Lady's Island, SC). This cantilever was 130 μm in length, 32.5 μm wide, and 1 μm thick, with a force constant of 0.6 N m^{-1} and a resonance frequency of 65 Hz. The typical radius of the n-type silicon tip was 8 nm with a full tip cone angle of 40°. Each resultant image was analyzed through Gwyddion software (version 2.44, Brno, Czech Republic).

2.3.4. Structural characterizations of 4D structures

To track the changes in the functional groups of 4D printed poly-Pickering-HIPEs, their structural characterizations were evaluated using Fourier-transform infrared (FT-IR) and ^{13}C-nuclear magnetic resonance (^{13}C NMR) spectroscopies. An FT-IR spectrometer (Jasco FT/IR6200, Tokyo, Japan) was used to determine the transmission infrared spectra of 4D structures. A solid-state of specimens required for the FT-IR assay was prepared in a pellet form using blending about 5 mg of each sample with dry potassium bromide (100 mg) [68]. Next, the samples were transferred to a pellet for scanning spectral area at a wavenumber of 400–4000 cm^{-1}, and 50 scans were recorded with a resolution of 1 cm^{-1}.

To further detect the changes in the structural properties of 4D printed poly-Pickering-HIPEs, a ^{13}C NMR was performed through a Bruker spectrometer (AvanceIII 500, Bruker, Ettlingen, Germany) equipped with a 4-mm MAS (magic angle spinning) probe, where frequency for carbons and protons was 75.46 and 300.13 MHz, respectively. The external reference glycine was utilized for the ^{13}C spectra and to set the Hartmann-Hahn matching condition in the cross-polarization experiments. The spectrum of each sample was obtained with the ramp $\{^1H\} \rightarrow \{^{13}C\}$ cross-polarization (CP)/MAS pulse sequence using the proton decoupling upon acquisition. The recycling period was 10 s and a contact time of 3 ms during CP was adjusted for all experiments. The SPINAL64 (small phase incremental alternation with 64 steps) sequence was employed for heteronuclear decoupling upon acquisition with a proton field H1H satisfying $\omega 1H/2\pi = \gamma HH1H = 62$ kHz. The spinning rate for all samples was 10 kHz.

2.3.5. Temperature-dependent behavior of 4D structures

To assess the effect of heating and cooling on the 4D structures Pickering emulsions, an AR 2000ex rheometer (TA Instruments, New Castle, DE) was used to evaluate small-amplitude oscillatory shear measurement, which was coupled with concentric cylinders (stator ID of 15 mm, 1 mm gap, immersed height 42 mm) and a Peltier temperature control unit. The elastic (G'), loss (G''), and complex (G^*) moduli were measured as functions of temperature (heating process from 10 to 85 °C and cooling process from 80 to 10 °C) at a heating or cooling rate of 1 °C min^{-1} in the strain-control mode with a strain amplitude of 1% and a frequency of 1 rad s^{-1} (within the *LVR* mentioned in Section 2.3.4).

2.3.6. Mechanical properties of 4D structures

The tensile stress–strain curves of rectangular 4D printed poly-Pickering-HIPEs were recorded using a uniaxial tensile tester (Instron 5569; U.K.) with a 10 N load cell at ambient conditions. The constant stretching rate was set at 50 mm min^{-1}. Regarding the tensile experiment, the specimens were cut into the dumbbell shape (35 mm in length, 14 mm in gauge length, 2 mm in width, and 1 mm in thickness). The constant stretching rate was fixed at 50 mm min^{-1}. The nominal tensile stress (σ_M) was considered as the force (F) divided by an initial cross-sectional area (S_0) of the specimens ($\sigma_M = F/S_0$). The tensile strain (ε)

was defined as a change in length (ΔL) divided by the original distance (L_0) of the specimens ($\varepsilon = \Delta L/L_0$). The elastic modulus ($E$) was measured by the slope of a linear area (within 5–15%) of the stress–strain curve. The toughness (U) was then obtained by an area of stress–strain plots as follows:

$$U = \int_0^{\varepsilon_{max}} \sigma_M d\varepsilon \quad (5)$$

Here, d is the width of the specimen and ε_{max} signifies the maximum strain the specimen experienced.

A successive loading–unloading tensile experiment was carried out to obtain hysteresis area by progressively increasing the strain until failure at 50 mm min^{-1} at a strain of 250%. Each specimen was initially stretched to the maximum strain of ε_1 and next unloaded. After returning to the initial length, the specimen was reloaded and stretched to an increased maximum strain ε_2 at the same velocity rate as the first loading and unloaded again. The loading–unloading operation was repeatedly performed on the same specimen with increased ε_3, ε_4,., ε_n until the specimen failed at an elongation break. The dissipated energy (U_{hys}) was measured in the loading–unloading circle according to Eq. 6:

$$U_{hys} = \oint \sigma_M d_\varepsilon \quad (6)$$

Regarding the tearing test, a trouser shape specimen (50 mm in length, 7.5 mm in width, and 1 mm in thickness) with an initial notch of 20 mm was stretched at a rate of 50 mm min^{-1}. The tearing fracture energy (G) was then obtained from Eq. (7).

$$G = (2F_{ave}/d) \quad (7)$$

where F_{ave} was a force of peak value upon steady-state tear and d was the specimen width. Each experiment was repeated at least three times.

2.4. Statistical analysis

All instrumental experiments were carried out as triplicate determinations and the mean and standard deviation of the data were reported. Analysis of variance (ANOVA) was utilized to determine the main effects of the examined independent factors and their interactions with the instrumental data. The measurements of all tests were analyzed in three and the mean and standard deviation of data were reported. Duncan's multiple range test was applied to separate means of data when significant differences ($p < 0.05$) were observed.

3. Results

3.1. Characterization of Pickering-HIPE-based inks

3.1.1. Droplet sizes and microstructures of Pickering-HIPEs

The evaluation of the size distribution change of the droplets in Pickering-HIPEs can offer a direct indication of the induced effect of long, flexible CNF (Figs. S-4 in Supplementary Materials) on the physical stability of the emulsion system. Fig. 1 illustrates the particle size distribution (*PSD*) and the relevant optical microscopy photographs of Pickering-HIPEs containing CNC (at a fixed level of 1.5 wt%) and different CNF concentrations. The *PSD* shows a wider range when CNF was added at a level < 0.6 wt% (PPH-0, PPH-2, and PPH-4 samples) because of the presence of droplet coalescence with bigger sizes. This could be due to a decreased extent of flocculation [60]. Similarly, the *PSD* of the system formulated by CNF concentration of > 0.8 wt% (PPH-10 sample) also shows significant coalescence and droplet size growth. Moreover, these Pickering-HIPEs could not stick to the glass vials to preserve their own gravity when the vials were placed upside down (Fig. 1). Conversely, *PSD* moved to the smaller droplet sizes once the CNF was incorporated at a level of 0.6 (PPH-6 sample) or 0.8 wt%

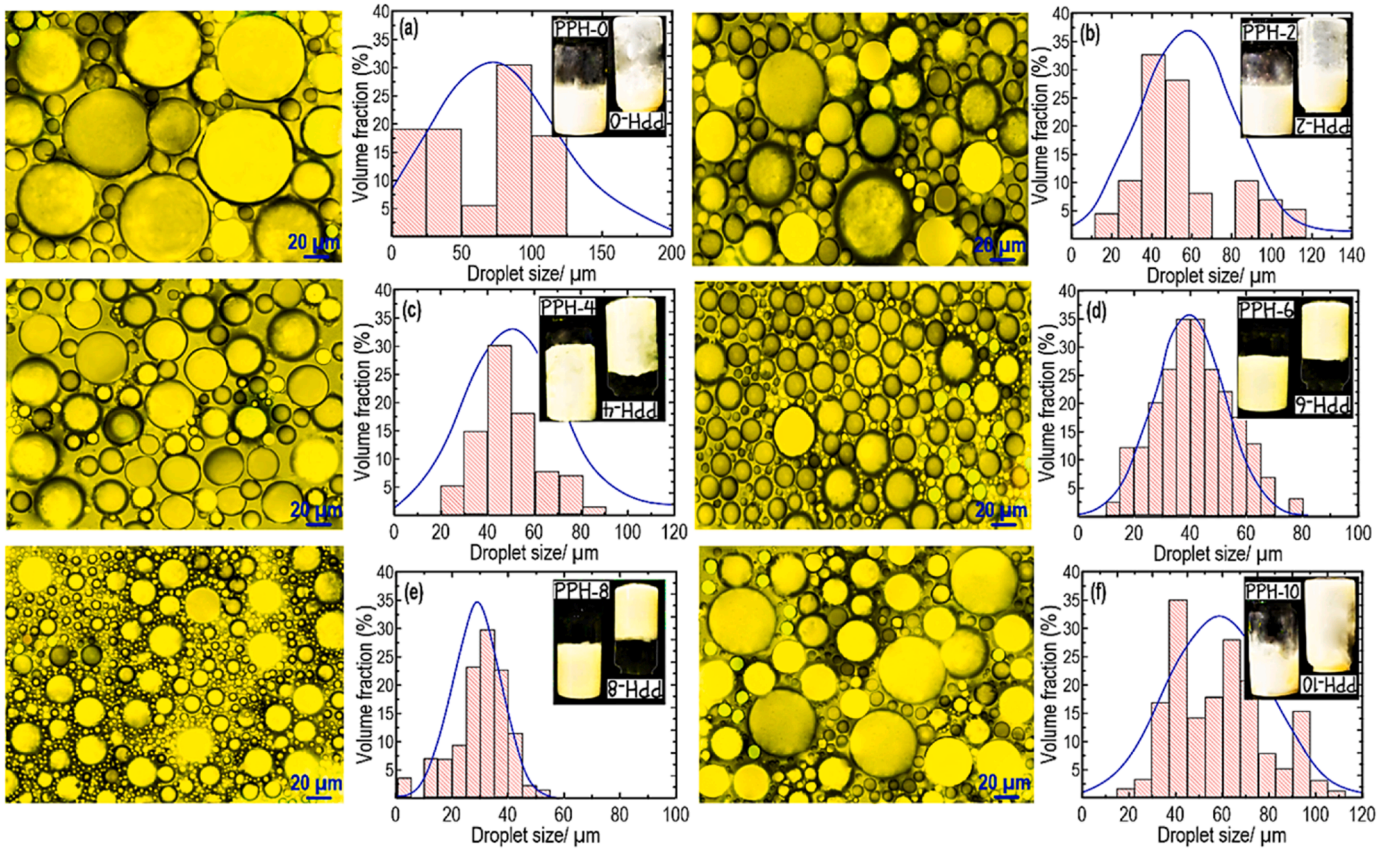

Fig. 1. Microscopic images and *PSD* results for different Pickering-HIPEs. (a): PPH-0, (b): PPH-2, (c): PPH-4, (d): PPH-6, (e): PPH-8, and (f): PPH-10.

(PPH-8 sample). In this case, the *PSD* of the systems reached a thinner range in these optimum levels of CNF. The small droplet size exhibits a higher stability of Pickering emulsions [70]. Therefore, the PPH-6 and PPH-8 HIPEs showed notable stability against coalescence with no sign of phase separation, which may be due to the occurrence of extensive flocculation (see Section 3.1.5). As a whole, incorporation of the optimum level of CNF into the CNC-included Pickering-HIPEs develops an emulsion with a minimal droplet change, which signifies the attendance of a synergistic effect of CNC and CNF on the HIPEs stabilizing [60]. In the current work, additional backscattering intensity and morphological evaluations were performed to detect if the MC/KC blend had a role in the physical stability of HIPEs (section S.3 in Supplementary Materials). The backscattering intensity profiles of HIPEs prepared by pure MC, pure KC, and a blend of MC/KC (with no CNC and CNF) showed the creaming occurrence of the oil droplets (Fig. S-3). This could signify there was a progressive increase in the particle size resulting from flocculation/coalescence. Thus, in this step, the HIPEs contained MC, KC, and MC/KC blend (with no CNC and CNF) didn't produce a gel-like structure to physically stabilize the system (as no crosslinker was used in this step).

The optical microscopy evaluation of the Pickering-HIPEs is also presented in Fig. 1. At CNF concentrations < 0.6 wt%, the system showed the existence of large discrete oil droplets in the Pickering-HIPEs, which might be owing to the coalescence of oil droplets. In contrast, the size of droplets obviously reduced in the systems with CNF concentration of 0.6 wt% or 0.8 wt% CNF. However, the presence of some flocculated droplets could also be observed from optical microscopy evaluation. On the other hand, the system with a CNF concentration of 1.0 wt% was composed of big and slightly flocculated drops. It was concluded that the CNC/CNF-stabilized Pickering-HIPEs can be stabilized through a depletion stabilization mechanism *via* the incorporation of sufficient levels of CNF [70].

3.1.2. Colloidal stability of Pickering-HIPEs

To study the colloidal stability of Pickering-HIPEs, the static multiple light scattering (S-MLS) measurements can assess the real-time stability or accelerated colloidal stability of the emulsion system according to the examination of particle size changes and particle migration phenomena [71]. Based on Eqs. 1 and 2, transmission (T) can be related to the volume fraction of droplets (φ) and the mean diameter of droplets (d), where a decrease in T could lead to a reduction of d, yet an increase of φ. Thus, to explore the dynamic colloidal stability of Pickering-HIPEs, as well as detect the emulsion droplet migration, the ΔT spectrum of the obtained emulsions stabilized by different levels of CNF were examined and the relevant results illustrated in Fig. 2 (Up). Here, the initial scanning transmission intensity is defined as a zero-line. In this case, the Y-axis shows the variation percent of the backscattering light intensity (ΔBS) compared with an initial state, whereas the X-axis displays the

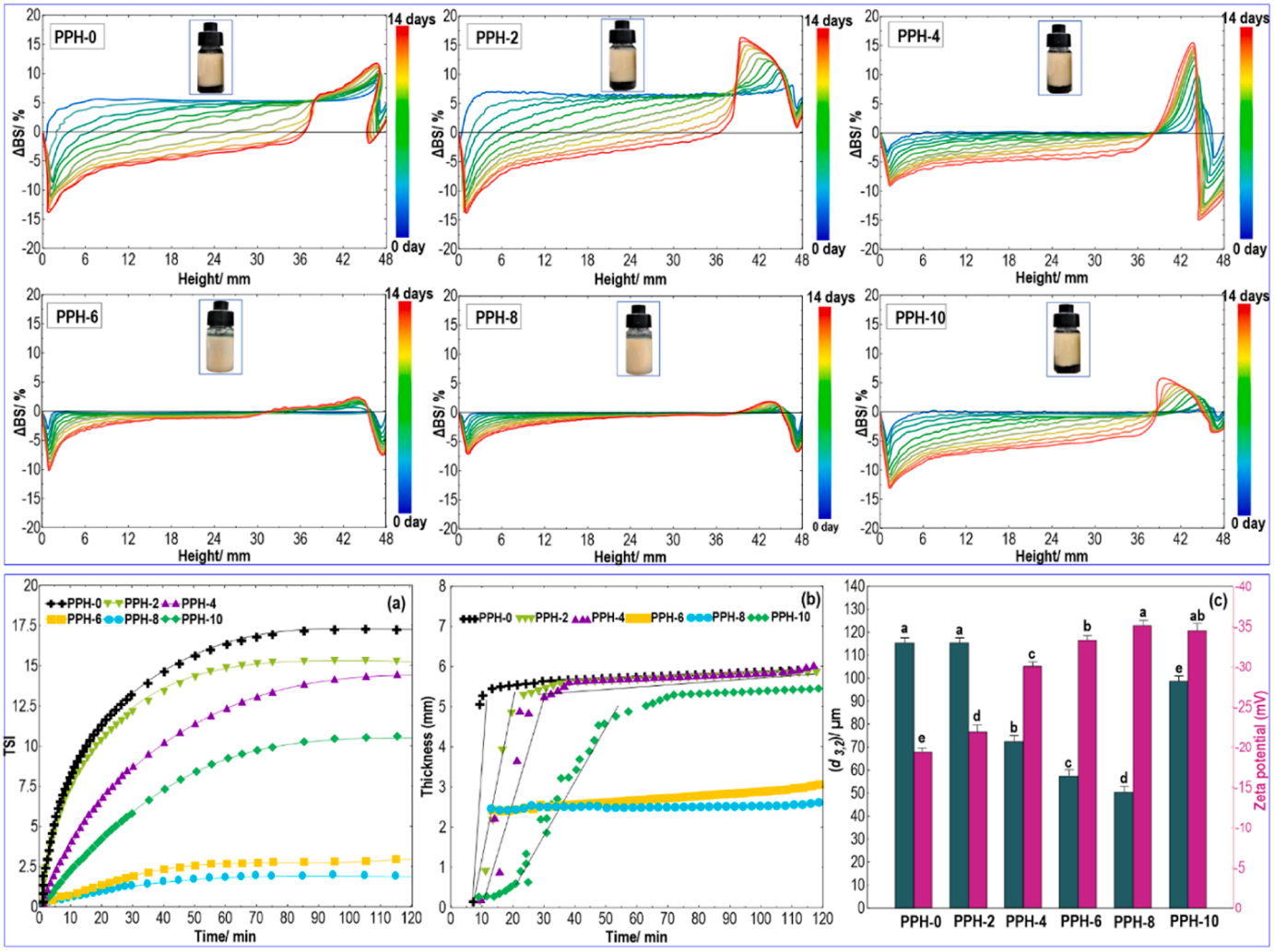

Fig. 2. (Up): Backscattering intensity profiles (Turbiscan) of different Pickering-HIPEs. The horizontal axis represents the height position along the test tube. All the samples were kept undisturbed at ambient temperature. (Down): (a) *TSI* plots, (b): Thickness plots, (c): ($d_{3,2}$) and ζ-potential, (b). Regarding ($d_{3,2}$) and ζ-potential, the means in each column with various letters (a–e) are significantly different ($P < 0.05$) according to Duncan's test.

height of the emulsion. The curves from blue to red also show the testing time of 0 to 14 days. In Fig. 2 (Up), all of the *BS* plots decreased with the increasing of time once the height was below 30 mm, representing a growth in the particle size. This could result from a coalescence of emulsified oil droplets [72]. However, the *BS* plots of PPH-6 and PPH-8 were less affected by droplet size growth. In the meantime, there was a notable reduction of *BS* for PPH-0, PPH-2, and PPH-4 once the height was below 5 cm during storage time. This clearly shows a reduction of the volume fraction of the dispersed phase, signifying the creaming occurrence of the oil droplets [72]. The larger droplets could possibly be migrated from the bottom to the top of the test tube owing to a density difference between water and oil. Similarly, Δ*BS* of PPH-10 notably reduced at the bottom but increased at the top of the tube over time, showing relatively poor stability. This proposes that the droplets progressively moved upward within the tube owing to gravity migration, resulting in the clarification at the bottom and creaming at the top (see the testing tubes in each Δ*BS* plot in Fig. 2, up).

Compared to other emulsion samples, the Δ*BS* values of the PPH-0 and PPH-2 increased about 5% below 3 mm and increased about 15% near 40 mm. This specifies that the bigger droplets move up, showing that the volume fraction has increased owing to the floating of oil droplets from the bottom to the top of the tube. Because of a broad distribution range of oil droplets (Fig. 1), their migration resulted from a density difference is apparent, which results in a quick aggregation and coalescence of droplets. As shown in Fig. 2 (up), the changes of *BS* plots concerning PPH-6 and PPH-8 samples were minor, showing slight change in the size of oil droplets during storage time. Therefore, droplet migration can greatly be delayed because of the synergistic effect of CNC and CNF. CNF may act to induce depletion stabilization of Pickering-HIPEs developed by interfacial adsorption of CNC [60]. This depletion effect, triggered solely by the non-adsorbing CNF, was achieved in the Pickering-HIPEs that contained spherical droplets and high-aspect cellulose nanorods.

TSI values of different Pickering-HIPEs were also measured and plotted as a function of time (Fig. 2a, down). *TSI* values show a two-area (increasing and plateau) behavior with increasing aging time. Compared to PPH-6 and PPH-8, the *TSI* plateau value of PPH-0, PPH-2, and PPH-4 (and even PPH-10) was higher. This indicates poor colloidal stability of these Pickering-HIPEs than those of other tested emulsions. Thus, it is clear that the incorporation of low concentrations of CNF could not notably affect the colloidal stability of Pickering-HIPEs. Consequently, as mentioned before, there was a clear separation of the extra aqueous phase in the testing tubes (oil droplets freely ascend) upon the impact of gravity, resulting in the development of a cream layer during storage (Fig. 2b, Bottom). PPH-6 and PPH-8, by contrast, offered increased flexibility and propensity for entanglement of the cellulosic fibrils at high concentrations, thereby forming dense networks in the aqueous phase [73].

To further explain the colloidal stability mechanism, the ζ-potential of the surface charge on the droplets was detected (Fig. 2c, Bottom). The electrostatic repulsions between the droplets are related to the degree of ζ-potential and, therefore, regulate the physical stability of emulsion systems. Typically, a more stable emulsion is associated with a higher ζ-potential [74–77]. A magnitude of about − 20, − 23, and − 30 mV was detected regarding PPH-0, PPH-2, and PPH-4, respectively, whereas the ζ-potential considerably decreased to around − 36 and − 39 mV for PPH-6 and PPH-8, respectively. This change is likely owing to the addition of more negatively charged groups into the systems. As CNF is negatively charged [78], there is more electrostatic repulsion (and also steric stabilization) in the system. Thus, the CNF at 0.6 and 0.8 wt% can effectively improve the colloidal stability of Pickering-HIPEs by increasing the magnitude of the surface negative charge, showing good protection against coalescence. These results well agree with the obtained difference in colloidal stability detected by the backscattering intensity profiles of Pickering-HIPEs.

The mean particle size was employed to quantitatively monitor the droplet size of emulsions (Fig. 2c, Bottom). The droplet size of the CNC-included HIPEs in the absence of CNF (PPH-0) was comparatively large with initial volume mean diameter ($d_{3,2}$) > 100 μm. This shows the presence of a high level of droplet coalescence in the system, which agreed well with the results of size distribution of Pickering-HIPEs (Fig. 1). With increasing the level of CNF, the droplet aggregates were notably smaller. Finally, the size of the droplet flocs increased after the addition of 1.0 wt% CNF, indicating that droplet flocs might be not strong in this emulsion (droplet aggregates were likely broken down to individual droplets after the application of shear force before size analysis). In this case, from the visual observation (Fig. 1) and backscattering tests (Fig. 2, up), this sample was physically unstable against creaming during storage, demonstrating the destabilization of Pickering-HIPEs induced by the introduction of 1.0 wt% CNF. These observations also were in accordance with the results of *PSD* and *TSI* experiments.

3.1.3. Static and oscillatory rheological response

Fig. 3a depicts the changes in the elastic (G') and viscus (G'') moduli of Pickering-HIPEs as a function of the amplitude sweeps. At the low strain values (<10%), all samples clearly presented a characteristic linear viscoelastic region (*LVR*). Following *LVR*, the occurrence of a yield or flow point (where viscoelastic moduli cross over) was detected by increasing the strain sweep. The strain sweep tests also showed the dominance of elastic modulus (G'_{LVR}) over the loss modulus (G''_{LVR}) within the *LVR* in all Pickering-HIPEs. This suggests that the Pickering-HIPEs had quasi-solid behavior with a gel-like structure at the lower oscillatory strain. In this case, the PPH-6 and PPH-8 showed higher G'_{LVR} and G''_{LVR} compared to other emulsions, in which the differences were over three orders of magnitude inside the *LVR* range. This is possibly associated with the development of a dense network in the aqueous phase due to increased flexibility and propensity for the cellulosic fibril's entanglement at 0.6 or 0.8 wt% CNF [78]. Another purpose of the oscillatory strain measurement was to detect the length of *LVR*. All Pickering-HIPEs presented a yield point near 1%, irrespective of the level of CNF. Though, following that yield point, the viscoelastic moduli of the emulsions, containing different levels of CNF, presented different *LVR* lengths. The systems formulated with CNF concentrations > 0.4 wt %, showed higher *LVR* length, where the G' and G'' reduced gradually after the yield points. However, emulsions with a CNF level of ≤ 0.4 wt % shifted the crossover point to the lower strain values. The length of *LVR* is the index of mechanical strength and shape preservation capability against the applied strains leading to structural deformation. This indicates the development of more structured and connected networks in PPH-6 and PPH-8 inks, which showed a more elastic gel-like system. Further increasing the CNF concentration to 1.0 wt%, a lowered G' and G'' value was obtained compared to the Pickering-HIPEs containing 0.6 or 0.8 wt%, which is likely due to a decreased number of droplets' flocculation.

Fig. 3b also illustrates frequency sweep measurements in *LVR* over a range of angular frequencies (0.1 −400 Hz). Regardless of the Pickering-HIPEs type, the $G'(\omega)$ values of emulsions were always higher than those of the $G''(\omega)$. This suggests the prepared emulsions had an elastic property rather than a viscous behavior [79,80]. Moreover, the elasticity of all Pickering-HIPEs was further obvious from the fact that both $G'(\omega)$ and $G''(\omega)$ values were moderately sensitive to the angular frequency, and no crossover point was detected at the frequencies from 0.1 to 400 Hz. In addition, with increasing the CNF level, the values of $G'(\omega)$ were considerably increased, which highlighted the existence of a strong gel-like structure with a mechanically stable network. As the CNF loading reaches 0.8 wt%, the elastic collision between those closely packed droplets inside a growing cluster was enhanced due to droplet flocculation (as shown in Section 3.1.5). Therefore, the long-term hydrodynamic interactions between the clusters rise suddenly likewise, with their increased sizes and numbers. It is then concluded that the emulsions could show optimal mechanical strength once the CNF

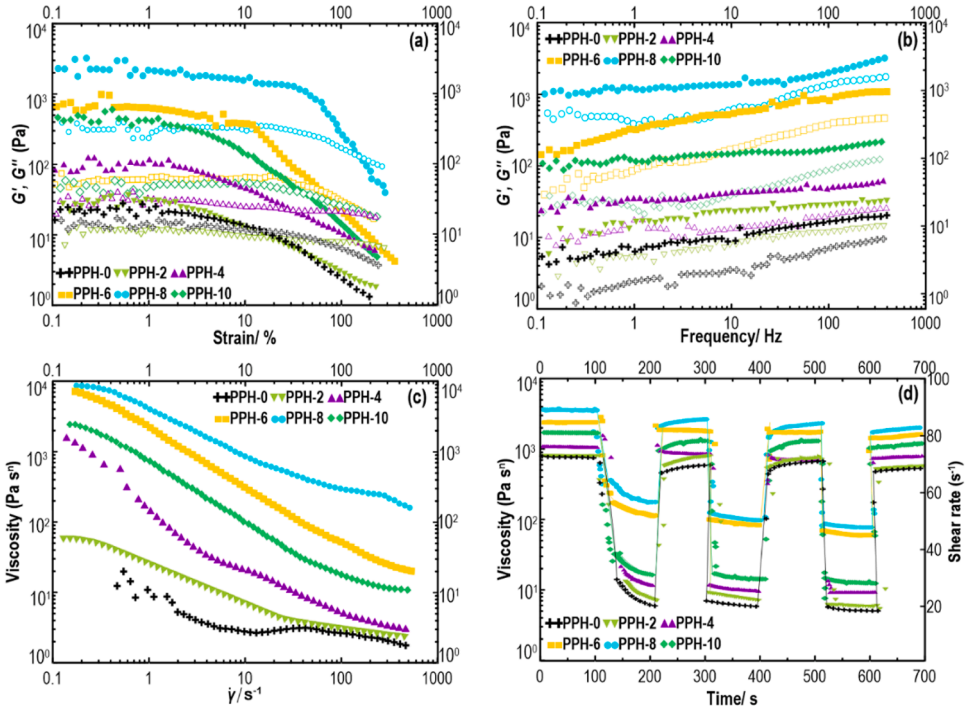

Fig. 3. (a): Amplitude sweep and (b): frequency sweep plots, where G' is solid symbols and G'' is open symbols; (c): Viscosity-shear rate curves; (d): The 5-ITT of different Pickering-HIPEs.

concentration was 0.6 or 0.8 wt%, which can offer some level of durability during the 3D printing process.

The steady flow behaviors of the Pickering-HIPEs were also measured since their obtained parameters offer beneficial insights into the flow behavior of 3D printing inks, which strongly affects the printing performance and shape fidelity [79]. Fig. 3c presents the changes in the apparent viscosity of the different samples as a function of shear rate. The rheological data exposed that the emulsions became more viscous with an increase in the levels of CNF. Again, the flow curves of samples with added CNF of 0.6 or 0.8 wt% offered the highest apparent viscosity. This is likely resulted from the contribution of flexible, but long cellulosic fibrils, which can develop interchain networks and can effectively interact in the aqueous region, thus increasing the viscosity.

3.1.4. *Time-dependent flow properties*

The five-interval thixotropy (5-ITT) experiment can be an efficient technique to simulate the impacts of shearing forces during 3D printing *via* generating quick alterations in shear rate [81]. To detect the influence of different levels of CNF on the thixotropic property of Pickering-HIPEs, their viscosity profiles as a function of applied shear rate and time are presented in Fig. 3d. In the initial interval, as expected, with increasing the level of CNF the viscosity of emulsions raised. In this case, the PPH-8 sample offered the highest viscosity values. Following the application of a high level of shear force (80 s^{-1}) in the second interval, the systems showed a shear-thinning behavior with a rapid reduction of viscosity. However, the decreasing trend for PPH-6 and PPH-8 samples occurred with a gradual slope. In the third or five intervals, the viscosity values of the Pickering-HIPEs were lesser compared to those of in the first interval, yet the PPH-0 or PPH-2 did not offer a reversible structure, and PPH-4 or PPH-10 samples only had a fair dynamic and recoverable network. This suggests that these emulsions might be improper for the 3D printing process due to the lack of restoration of their initial structures after destruction [75]. The higher thixotropic restoration is positively associated with upholding the mechanical strength of an emulsion following the printing process in addition to ensuring an accurate printing object. For this reason, and in accordance with viscoelastic results, both PPH-6 and PPH-8 can be more appropriate for 3D printing due to their highly dynamic and recoverable structure. Therefore, a weak CNF network developed in the aqueous phase at a given amount promoted depletion stabilization by offering the elastic features of CNF to kinetically limit the flexibility of flocculated droplets.

3.1.5. *Confocal images of the top layer of Pickering emulsions*

To further analysis of the interfacial framework, the network microstructure in the top layer of Pickering-HIPEs was performed through CLSM (Fig. 4). It is worth noting that no discussion associated with the oil levels should be performed according to the number of oil droplets detected by the CLSM photomicrographs as they are affected by the used emulsion preparation for imaging. The oil droplets on the top layer of the Pickering-HIPEs including CNF with a concentration of < 0.6 wt% were homogeneously distributed, yet some local droplet flocculation was detected. This also shows that droplet clusters or flocs were not strong in the emulsions (they may be broken down to separate droplets during shear forces). These results can indicate the presence of rather a regular creaming separation, which verifies that CNF at the lower concentrations had negligible impact on the emulsion phase behavior. This is possibly elucidated since the low concentrations of CNF did not induce the development of an interfacial network, with less impact on the viscosity-stabilizing behaviors (see oscillatory rheological data in Section 3.1.3).

Contrary, the Pickering-HIPEs containing a CNF concentration > 0.4 wt% show a clear droplet aggregation. The degree of droplet flocculation increased with increasing CNF level, where the droplets attained the maximum amount of flocculation in the emulsions including 0.8 wt% CNF. In contrast to the visual observations (Fig. 1), the CLSM showed outstanding alteration of creaming properties with the oil droplet flocculation. Considering the obtained data, it could be concluded that the droplet aggregation process is governed by depletion effects, produced by interfacial adsorption of CNC after a critical aggregation concentration of CNF was attained. It was reported that showed that the microstructure of aggregate droplets became

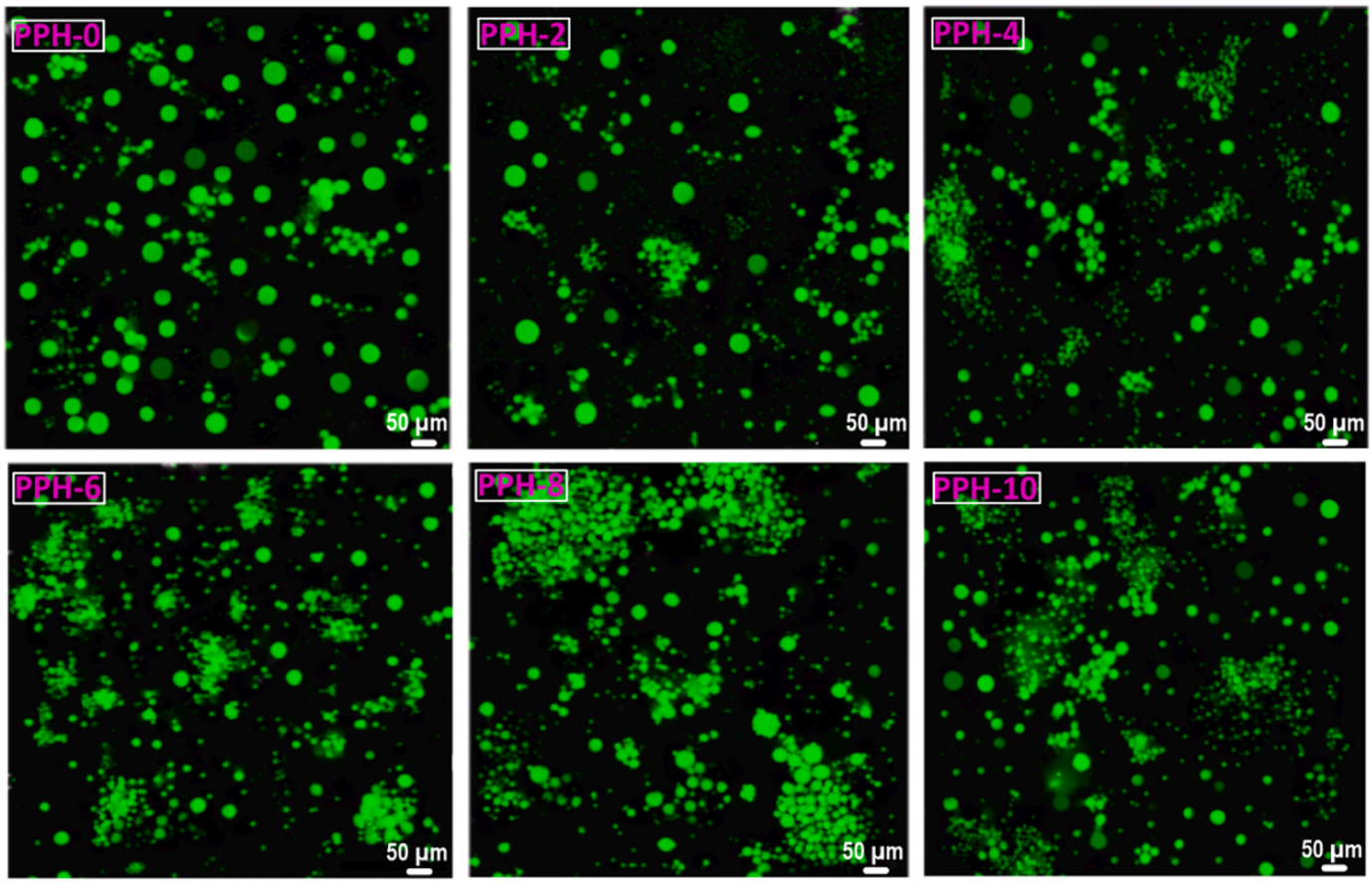

Fig. 4. Confocal images of the top layer for different Pickering-HIPEs. The oil phase was stained with Nile red. All the samples were stored at ambient temperature.

independent of CNF level above the critical stabilization concentration, with two characteristic regions: depletion flocculation (at 0.1 and 0.2 wt % CNF) and gel development (>0.3 wt% CNF) [75]. In the current work, the produced attractive interactions can be obtained by the elimination of the CNF from the confined regime near the oil droplets, which produces an attraction between droplets. If the developed attractive forces are adequately strong, droplet flocculation will be promoted.

3.1.6. QCM-D analysis

A QCM-D was conducted to characterize the adsorption-desorption behaviors and interfacial adsorption properties at the O/W interface (Fig. 5). The frequency (Fig. 5a) and dissipation shift (Fig. 5b) of different samples on the sensor as a function of time are two main important parameters obtained from QCM-D analysis [82]. A higher frequency value proposes that more mass is adsorbed onto a hydrophobic surface. The dissipation offers data regarding the adsorbed film features in a hydrophobic surface, developing a stiff film containing low water content (low dissipation) or a water-rich soft film (high dissipation) [83]. A sudden decline of $\Delta f/n$ (Fig. 5a) and a sharp rise of ΔD (Fig. 5b) were detected for all Pickering-HIPEs during the initial adsorption process. This is likely associated with a quick deposition of CNF (along with CNC) onto the hydrophobic phases upon injection into the QCM-D instrument. After that, a gradual reduction of $\Delta f/n$ or a slow upsurge of ΔD at longer times could be detected. This behavior is likely consistent with the slower deposition of CNF/CNC since the adsorption places were almost occupied and some nanofibrils/nanoparticles adsorbed onto the already developed interfacial layer. Some works stated that a similar decreasing trend of $\Delta f/n$ once more amphiphilic compounds were incorporated [84]. This result could be partly because of a decrease in adsorption places and partly related to multilayer development by the CNF/CNC. In this case, the ΔD value decreased and the $\Delta f/n$ values increased after rinsing the interfaces with the buffer solution, though they did not go back to their initial states. This phenomenon may be assigned to the elimination of weakly bound or some unbound nanofibrils/nanoparticles from the interface, resulting in viscoelasticity reduction.

The slope of ΔD and $\Delta f/n$ (ΔD-Δf plot) was measured to monitor the viscoelasticity of the adsorbed layer of CNF or CNC through the different phases of adsorption/desorption (Fig. 5c and d). A small slope is related to a more rigid and dense interfacial layer, while a large slope is associated with a soft and viscoelastic one. A conformational change can occur in the adsorption layer when an inflection point at the ΔD-Δf curve happens through the adsorption/desorption process. On the contrary, if the ΔD-Δf plot remains constant, there is no occurrence of conformational change of the adsorption layer. During adsorption, the slopes of the ΔD-Δf plot were considered as K_1 and K_2 (Fig. 5c), and during desorption, the slopes were defined as K_3 and K_4 (Fig. 5d). There is an inflection point in the slopes of ΔD-Δf plots regarding all samples during the adsorption/desorption process. Obviously, before the inflection point, a quick kinetic was detected, yet a slow kinetic occurred after this point, which is related to the development of a multilayer adsorbed layer [83]. During initial adsorption, the K_1 values were higher for Pickering-HIPEs having CNF at a concentration of < 0.6 wt% (Table 1), which proposed the presence of a soft adsorbed layer. During rinsing, a sudden reduction of K_4 values was associated with the desorbing of loosely bound nanoparticles from the sensor surface; accordingly, there is the development of a stiff interfacial layer. The value of K_4 was maximum for the PPH-6 and PPH-8 samples, proposing the formation of the more viscoelastic interfacial layers. This could be related to the development of interchain networks as affected by the presence of more flexible cellulosic fibrils, which efficiently interacted in the aqueous phase, therefore enhancing the viscoelastic properties of

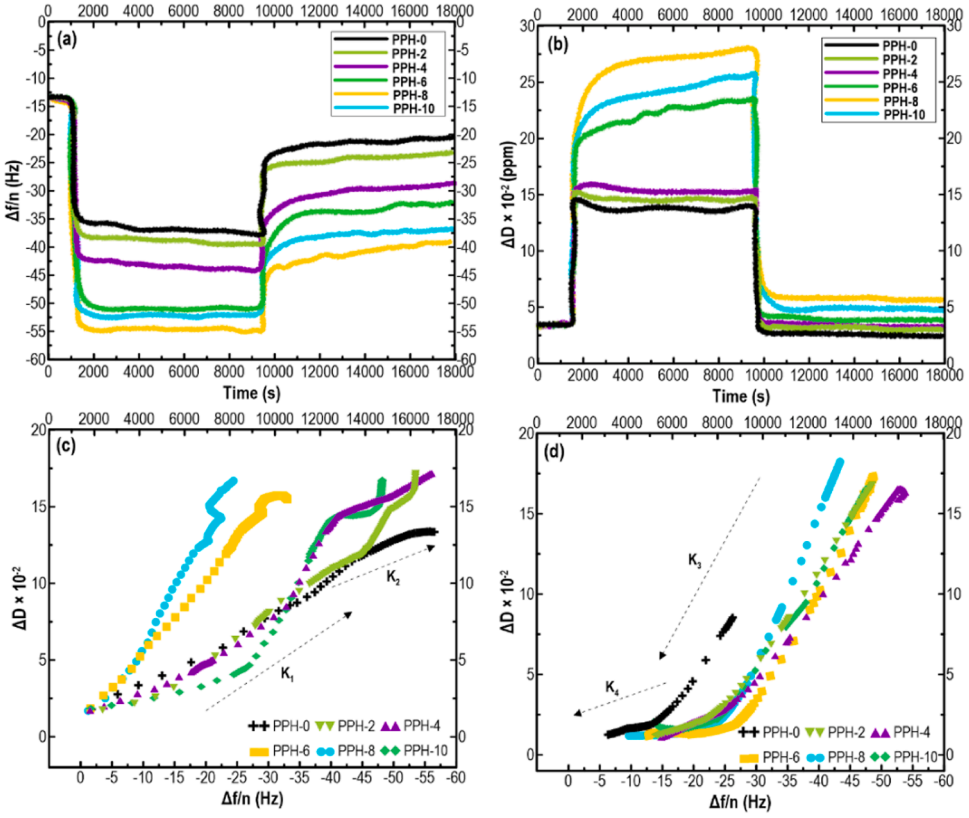

Fig. 5. The adsorption-desorption kinetics of Pickering-HIPEs at the O/W interface. (a): Δ*f* and (b) Δ*D* from the third overtone as a function of time during adsorption and desorption. *ΔD-Δf* plots during (c) adsorption and (d) rinsing processes.

Table 1
Slopes of ΔD-Δf plots from the third overtone for Pickering-HIPEs during adsorption/rinsing at the hydrophobic gold surface.

Sample	$K_1 \times 10^4$ (Hz^{-1})	$K_2 \times 10^4$ (Hz^{-1})	$K_3 \times 10^4$ (Hz^{-1})	$K_4 \times 10^4$ (Hz^{-1})
PPH-0	0.247 ± 0.013^{a}	0.078 ± 0.009^{c}	0.256 ± 0.007^{b}	0.112 ± 0.017^{a}
PPH-2	0.223 ± 0.012^{c}	0.106 ± 0.013^{a}	0.238 ± 0.009^{a}	0.105 ± 0.009^{a}
PPH-4	0.207 ± 0.01^{b}	0.152 ± 0.014^{d}	0.318 ± 0.016^{b}	0.167 ± 0.019^{a}
PPH-6	0.112 ± 0.013^{bc}	0.226 ± 0.015^{b}	0.480 ± 0.022^{c}	0.179 ± 0.018^{b}
PPH-8	0.095 ± 0.017^{bc}	0.270 ± 0.016^{b}	0.534 ± 0.019^{c}	0.205 ± 0.011^{b}
PPH-10	0.198 ± 0.013^{bc}	0.189 ± 0.017^{b}	0.439 ± 0.009^{c}	0.137 ± 0.024^{b}

The means in each column with various letters (a–e) are significantly different ($P < 0.05$) according to Duncan's test.

the interfacial layer.

3.2. HIPEs to poly-HIPEs: Characterization of 4D printed objects

3.2.1. Printing quality and thermo-responsive of 3D printed objects

Since the PPH-8 ink displayed superior colloidal stability, better thixotropic features, and improved mechanical strength, leading to the development of a strong gel-like network, it was considered to be an appropriate candidate for the 3D printing process and worthy of further investigation. However, the printing performance of PPH-0 ink was also provided to give a better comparison between this sample and the superior ink (*i.e.*, PPH-8). Moreover, it should be mentioned that we did not include the printing quality images of PH-C (poly-HIPE that induced MC/KC with 0.08 wt% CNF and 1.5 wt% CNC, but with no crosslinker), in which it could not produce a well-defined scaffold due to a weak structure with poor shape-fidelity. However, its structural properties, thermo-responsive mechanism, and mechanical strength have been included in the subsequent sections (Sections 3.2.2–3.2.4).

In this work, poly-Pickering-HIPEs were effectively developed through *in-situ* crosslinking of Pickering-HIPE-based inks during hot-melt extrusion-based 3D printing, which produced a series of 3D printed structures. A series of printed structures from 1D to 3D formulated by PPH-0 or PPH-8 ink is shown in Fig. 6 (Top). The diameter of the 1D filament printed by PPH-8 ink is about 510 μm (Fig. 6 Top, *i*). Besides, the cross-sectional image of its rupture surface was smooth and circular (Fig. 6 Top, *ii*), which could lay the superior basis for more intricate objects. In contrast, the surface and cross-section of the rupture surface regarding the filament printed by PPH-0 ink were rough with several irregularities. The 2D square lattice and 3D self-supporting scaffold (with multiple layers) of PPH-8 ink also evidenced superior printing performance (Fig. 6 Top, *iii*). The 2D square lattice object printed by PPH-0 ink, by contrast, showed a shape deformation with curve-like angles, proposing dimensional instability. Similarly, its 3D self-supporting scaffold had an irregular and coarse matrix with inferior printing quality and poor dimensional stability (Fig. 6 Top, *iv*). This also led to some levels of extension of the line-edge roughness compared to a 3D structure printed with PPH-8 ink. As mentioned earlier, the development of a gel-like structure in PPH-8 could explain this difference in precise geometry and shape fidelity. In this case, an improved elastic modulus with higher thixotropic behavior as affected by increasing the degree of droplet flocculation led to its better spatial resolution and printing performance. Fig. 6 Top (*v*) also shows the FE-SEM microstructures of 3D self-supporting scaffolds printed by PPH-0 and PPH-8 inks. In this case, the development of a high-level porous structure concerning a 3D self-supporting scaffold printed by PPH-8 ink was

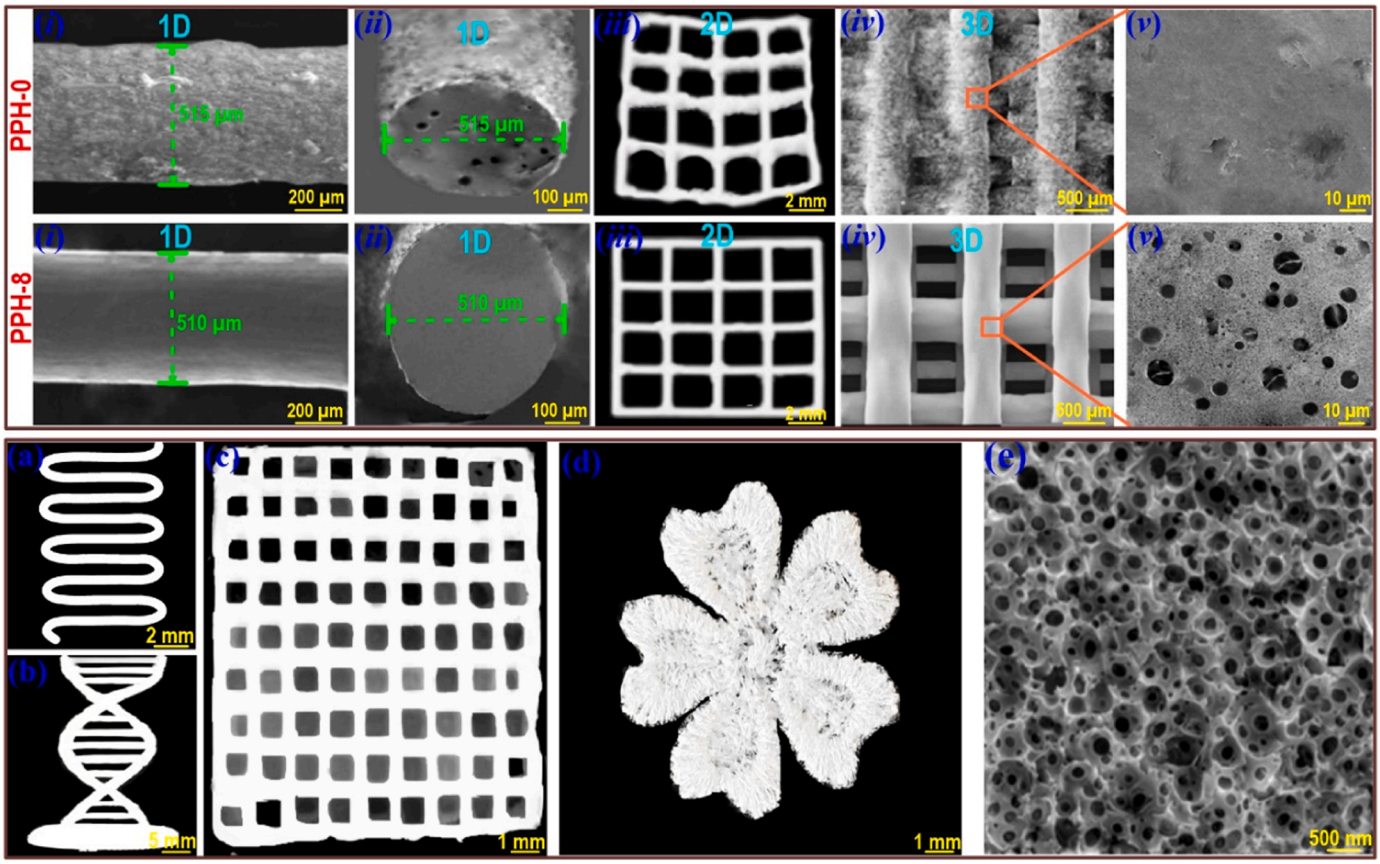

Fig. 6. Printability of different printed constructs from 1D to 3D developed by PPH-0 and PPH-8 inks. (Up): FE-SEM images of *(i)* the surface of 1D printed filaments, *(ii)* their relevant cross-section rapture, *(iii)* 2D square lattice, *(iv)* 3D self-supporting scaffolds and *(v)* microstructures of 3D self-supporting scaffolds. (Down): Printing quality of 3D printed objects developed by PPH-8 ink. (a): 1D zigzag pattern; (b): 3D DNA helix; (c): 3D square lattice, (d): 3D flower with 5 petals, and (e): magnified FE-SEM image of Fig. 6 Up (*v*) for PPH-8.

detected. It also offers a uniform structure in terms of orientation and shape of spaces. Yet, the surface morphology of the 3D self-supporting scaffold produced by PPH-0 was characterized by some level of irregularity and heterogeneous structure with no porous matrix. Compared to the droplet sizes of its ink, PPH-8 poly-HIPE had comparatively larger pore sizes. During the preparation of the 4D printed structure, oil removal and drying processes were performed to prepare poly-Pickering-HIPE. During these processes, the size of the oil droplet may be increased. Therefore, the pore size of the as-prepared 4D object was slightly bigger in comparison with the diameter of the associated Pickering-HIPE-based ink. It has been reported that the pore size of 3D objects is related to the oil removal and drying process of the precursor emulsion-based inks [34].

Fig. 6 (Bottom) presents the printed structures of a 1D zigzag pattern, 3D square lattice, 3D DNA helix, and a flower with 5 petals as well as its FE-SEM photomicrographs developed by PPH-8 ink. All the obtained printed architectures offered superior printing quality and universality to printed constructs from 1D to 3D and micro to macro size. The printing process of PPH-8 ink offered the development of well-defined printed constructions, which were self-supported with the ability of shape retention. Moreover, the geometric structure of the printed constructs was also suitably upheld with no apparent cracking, distortion, and volume shrinkage. The application of the gel-like PPH-8 ink with greater shear elastic modulus and improved yield strength reserved the printing filamentary shape. The FE-SEM image of the 3D flower manifests that there is the development of high levels of 3D interconnected porous structure with blurry sieve-like shape, which included numerous aperture diameters in micro to nanometers size. The small voids in the interconnected macroporous structures displayed average void diameters ranging from 200 nm to 3 µm. This result proposes excellent consistent relationships with the size distribution of the droplets poly-Pickering-HIPEs.

The shape recovery feature of the printed PPH-8 object under heat stimulus was evaluated according to its quantitative shape-memory properties and good printability (Fig. 6). By integrating the 3D printing performance with the shape-memory feature of heat stimulus printed PPH-8 structure, different printed constructs with 3D permanent shapes were obtained concerning the restoration of their structures with the trigger of temperature. A printed “butterfly” and “flower” objects were printed to approve the arbitrary transformation between permanent and temporary 3D shapes (Fig. 7).

Fig. 7 (Top) and Fig. 7 (Bottom) present several temporary shapes of the “butterfly” and the “flower”, respectively. In the printed butterfly, after being fixed into a temporarily deformed shape, the butterfly presents a sequential recovery upon heating. The recovery of the printed flat flower with different petals folded into its initial temporary and original shape in the sequence was also taken into account. The folded flowers were distorted into different transitional phases, in which some petals open while some closed in a temperature ranging from 15–45 °C. The flat flower altered its shape in sequence during continuous reheating up to 90 °C. It has been reported that MC and KC-contained nanomaterials can develop thermo-responsive poly-Pickering-HIPE-based gels (with temperature-dependent sol–gel transitions from 40 to 80 °C [63,64,67]. From this demonstration, it is concluded that the 3D printed objects (which are regarded as 4D printed objects hereafter) showed a clear shape memory impact, and intricate shape transformation among different topological 4D structures was effortlessly manipulated. The shape recovery of the flower was completed once the petals opened up at

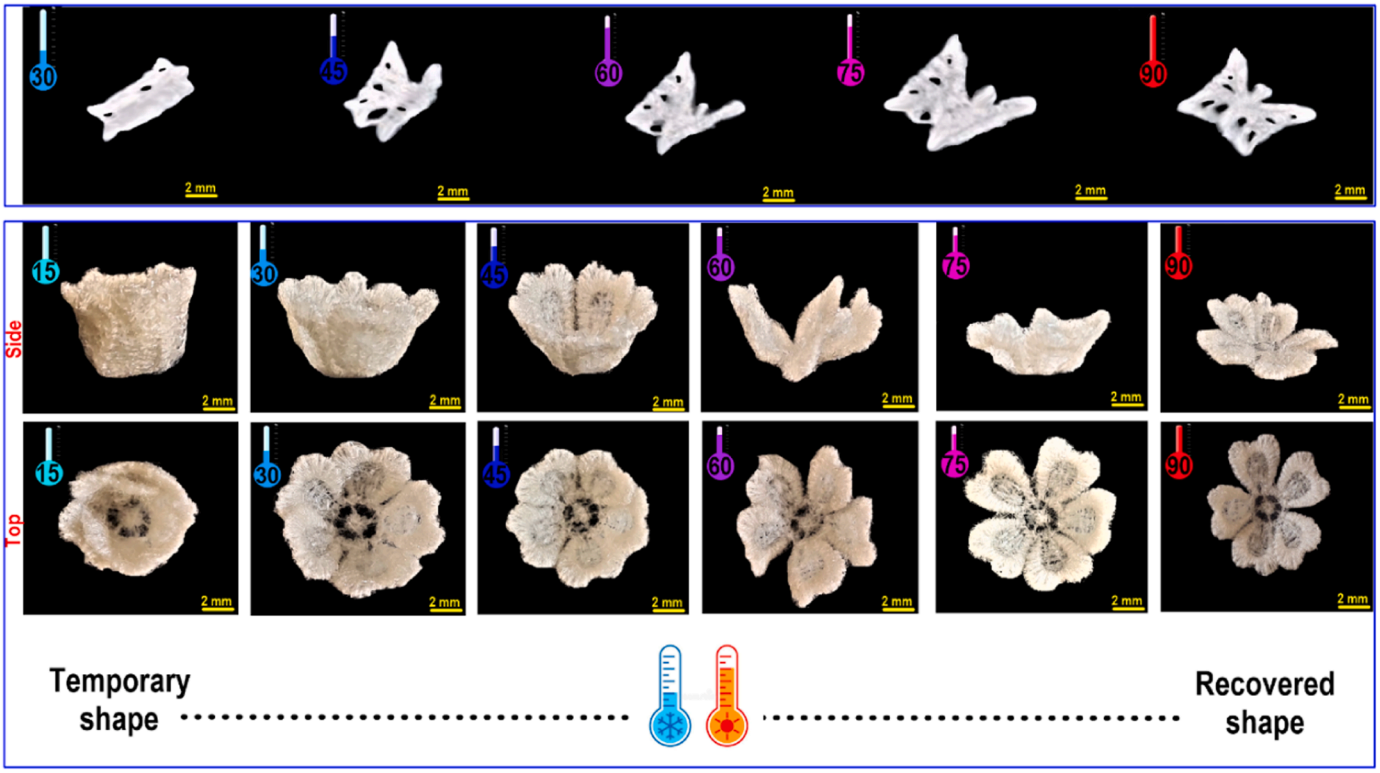

Fig. 7. Sequential shape memory response of 4D printed PPH-8 object as affected by temperature changes. (Top): The arbitrary transformation between permanent and temporary 3D shapes of printed "butterfly" and (Bottom): "flower with 5 petals". Each shape includes a thermometer graphic, which monitors the temperature of the atmosphere.

higher temperatures, which reflects the constant shape-changing ability according to the shape memory effect.

The overview of the preparation of 4D printed thermo-responsive porous construct is shown in Fig. 8. Preparing the 4D poly-Pickering-HIPEs involves four main elements: continuous water phase, dispersed oil phase, particulate (*i.e.*, Pickering)-type emulsifier, and crosslinker. The oil phase (75% volume fraction) was dispersed into a continuous water phase (25%) containing MC/KC aqueous dispersion stabilized by CNC/CNF hybrid, which produced Pickering-HIPE-based ink (Fig. 8a,d). MC and KC were chosen as they are water-soluble and thermo-responsive polymers, which can exhibit temperature-dependent sol–gel transitions in the temperature range of 60–80 °C. Before 3D printing, the hydrophilic crosslinking agent (MBA) was added to the prepared Pickering-HIPE-based ink. We hypothesized that the Pickering-HIPE-based ink was able to produce a thermo-responsive construct owing to the thermoresponsive nature of both MC and KC. The 3D printing of Pickering-HIPE-based inks, in the presence of a crosslinker, produced poly-Pickering-HIPEs by *in-situ* crosslinking of MC/KC. During hot-melt extrusion-based printing, the crosslinking of the continuous phase of HIPE was performed by MBA, which may crosslink two biopolymer chains through the hydroxyl groups present at both ends and supports to form a 3D network. Specifically, during the chain crosslinking, the end acrylate groups of MBA can react with the active hydroxyl groups of biopolymers to form a crosslinked structure (Fig. 8b,e). The hydrophobic association forms a hydrogel network that further immobilizes the oil droplets. After 3D printing, the 4D printed poly-HIPE structure was developed through oil removal and freeze-drying (Fig. 8c,f). When the temperature was lower than the LCST, the intramolecular bonds of poly-HIPEs can develop the hydrated hydrogen bond to delay the LCST, while once the temperature increased to above LCST, the intramolecular bonds could bind other intramolecular linkages to trigger the intermolecular aggregation, as displayed schematically in (Fig. 8g,h,i).

3.2.2. *Structural characterizations of 4D printed objects*

This section is dedicated to describing in-depth the molecular and structural properties of 4D printed scaffolds using FT-IR, ^{13}C NMR, water contact angle, and AFM measurements. Following this section, the thermo-responsive mechanism and mechanical properties of 4D-printed objects are considered. The changes in the chemical structures of PH-C, PPH-0, and PPH-8 were detected by FT-IR experiment, and the resulting spectra are shown in Fig. 9a. After 3D printing of PH-C, its relative FT-IR characteristic peaks were detected not to be changed, nor were found the appearance new bands compared to MC/KC blend (to track the FT-IR spectrum of MC/KC blend, see section S.1 in Supplementary Materials). This emphasizes that the incorporation of CNC (1.5 wt%) and CNF (0.08 wt%) without adding MBA followed by 3D printing did not affect the structural integrity of the MC/KC in the PH-C scaffold. The FT-IR spectrum of PH-C shows a distinguished peak around 1661 cm^{-1} (related to C═O stretching). After the formation of the crosslinked network (PPH-0 and PPH-8), the peak position of C═O was found to be slightly shifted to 1698 cm^{-1} due to the crosslinking action of MBA (Fig. 9a). Some works highlighted a shifting in the intensity of C═O band after MBA crosslinking of a blend of KC [66]. Compared to PH-C, FT-IR results specify the disappearance of characteristic bands at about 1565 (attributed to C═C stretching) and 988 cm^{-1} (assigned to =CH out of-plan- bending), which may refer to a complete crosslinking [68]. Furthermore, the FT-IR spectra of PPH-0 and PPH-8 show the appearance of a robust peak at 1691 cm^{-1} (attributed to the C═N stretching vibration) and the emergence of two new peaks at 1521 and 1116 cm^{-1} related to the N–H bending vibration of the -NH_2 group and the C–N stretching vibration, respectively [69].

A solid-state ^{13}C NMR spectroscopy was further used to qualitatively confirm the crosslinking process of the continuous phase of HIPEs (Fig. 9b). A characteristic band of cellulose type '*I*' (*i.e.*, C_1: 104.7 ppm, C_4: 90.2 ppm, $C_{4'}$: 89.4 ppm, group C_2–C_3–C_5: 71.0–81.2 ppm, C_6: 68.2 ppm, and $C_{6'}$: 65.7 ppm) was noticed for PH-C [76]. After the

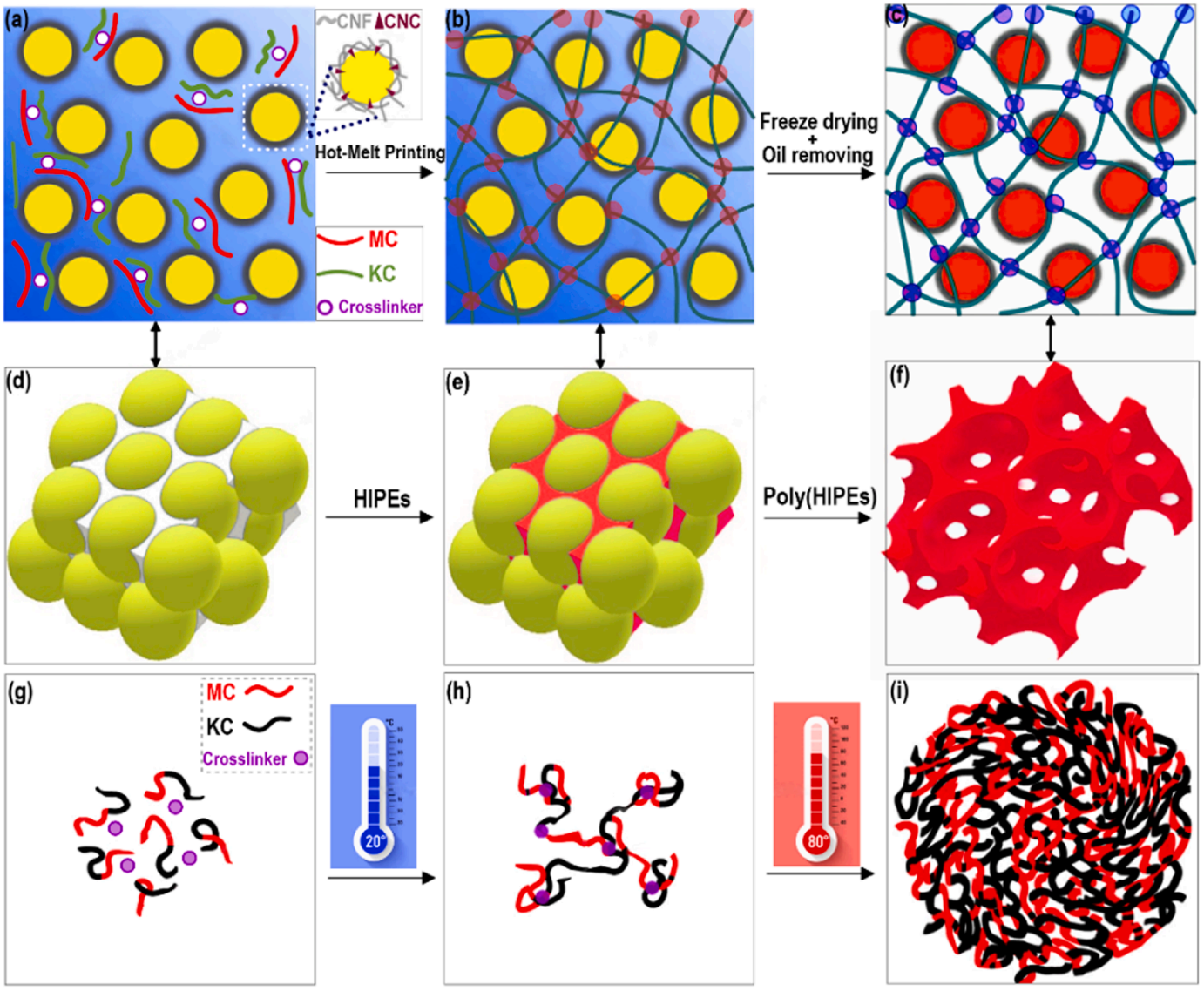

Fig. 8. Overview of the preparation of 4D printed thermo-responsive porous construct. (a,d) Preparation of Pickering-HIPE-based ink, which includes dispersed oil phase and continuous water phase (MC/KC with CNC and CNF along with crosslinker). (b,e) As-prepared Pickering-HIPE-based ink after *in-situ* crosslinking during 3D printing. The thermo-responsive shape-memory porous construct contains oil droplets that are stabilized by both the CNC and CNF, as well as hydrophobic association. (c,f) The poly-HIPE structure is formed by oil removal and freeze-drying after 3D printing. The crosslinked network junctions are presented as red points. (g, h,i) Schematic diagram for changes in the average hydrodynamic diameters of the MC/KC filaments in poly-HIPEs.

synthesis of PH-0 and PH-8, the characteristic peaks (C_1-C_6) of cellulose type '*I*' remained in these samples. However, there is the appearance of chemical shifts of the carbon atom of -CH_2- and C═O related to MBA [80] around 35 and 161 ppm, respectively. The latter result can be consistent with the carbonyl stretching vibration around 1698 cm^{-1} detected by FTIR assay (Fig. 9a). According to the literature, there is also no indication regarding the chemical shift of carbon atom of MBA corresponding to the -CH═ ranging from 125–135 ppm [80]. This can show the occurrence of a crosslinking reaction between MBA and MC/KC. Combined with the results of FTIR, it is also possible that the signal at 35 ppm may be ascribed to the carbon on the -CH_2- group produced by the addition reaction of -CH═ [80]. It should be pointed out that the characteristic peaks of C_4 and C_6 (assigned to cellulose type '*I*') presented a greater resolution loss in the case of PH-8. This is likely associated with lower mobility of carbons of anhydrous D-glucose units resulting from the crosslinking of MC/KC with MBA [86]. These changes suppose the crosslinking of the continuous phase of HIPEs affected by MBA during the hot-melt 3D printing process.

Likewise, a model poly-Pickering-HIPEs thin film was prepared using a spin-coating method (section S.1.2 in Supplementary Materials) to assess the sessile drop water contact angle assay. Fig. 9c shows PH-C film possessed a high hydrophilicity property, representing a low water contact angle of $\theta = 48.3^{\circ}$. This specifies that the polymeric backbone of the MC/KC blend showed a moderately wettable character. However, the contact angle of PH-C presented a higher value compared to MC/KC film (with no added CNC and CNF) (section S.1.2 in Supplementary Materials). This was expected as PH-C included CNC (1.5 wt%) and CNF (0.08 wt%), which offer a certain level of hydrophobicity for the PH-C matrix. By contrast, the surface hydrophobicity of PPH-0 and PPH-8 showed a much higher value than that of PH-C film. This is likely associated with the development of intermolecular interactions between MC and KC due to the application of MBA crosslinker during the 3D printing process. The crosslinking method imparts the produced 4D printed poly-Pickering-HIPEs with improved surface hydrophobicity and enhanced matrix rigidity (data not shown). The obtained data further supported the effective *in-situ* crosslinking process of Pickering-

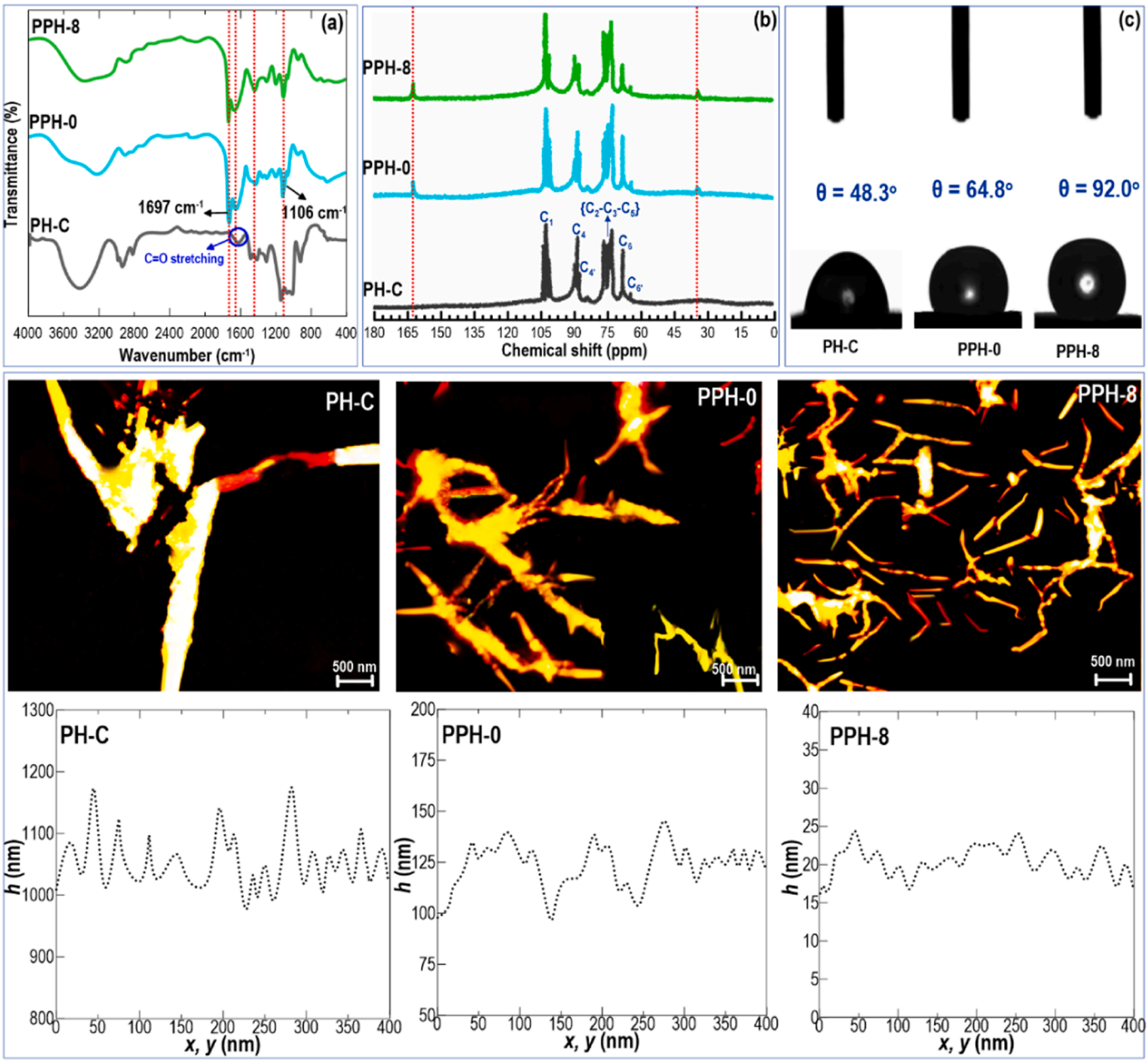

Fig. 9. Top: (a) FT-IR, (b) solid-state ^{13}C NMR, and (c) contact angle images of PH-C, PPH-0, and PPH-8. For the contact angle test, a thin film of each sample was fabricated through a special spin-coater (section S.1.2 in Supplementary Materials). Middle: High-magnification AFM images of PH-C, PPH-0, and PPH-8. Bottom: The typical height profiles along the long axis of samples show clear variations in height along the axis for PH-C, PPH-0, and PPH-8.

HIPEs, which developed poly-Pickering-HIPEs.

By taking advantage of AFM using the SPM-based method, the microstructure of PH-C, PPH-0, and PPH-8 at 80 °C was examined (Fig. 9-middle). The PH-C was assembled into micrometer-long scaffolds that are > 12 μm in diameter. Along the long axis of the scaffold, there was a clear modulation in the height profile, reminiscent of other twisted assemblies. The AFM data for PPH-8 (or somewhat concerning PPH-0) was qualitatively different (Fig. 9-bottom). These 4D printed poly-Pickering-HIPEs formed scaffolds that were ~1.0 μm in diameter, which were prominently shorter and thinner with some ramified chains, though some isotropic aggregates are also observed.

3.2.3. *Thermo-responsive behavior of 4D printed objects*

The mechanical properties of MC [85], KC [87], and their blend system [88] strongly depend on temperature, where they show lower critical solution temperature (LCST) in water [88]. The viscoelastic transition, including elastic and loss moduli (G″ not shown), is readily detected by linear dynamic mechanical spectroscopy experiment and the obtained results are illustrated in Fig. 10. The elastic modulus (G') at 1 Hz plotted against temperature (T) for which 4D printed objects of PH-C, PPH-0, and PPH-8 were heated and subsequently cooled (Fig. 10a). As can be seen, the G' (T) values changed with temperature during heating-cooling cycles. The results show that upon heating, the G' (T) was increased with increasing temperature up to 80 °C, in good agreement with the dynamic mechanical spectroscopy results previously reported by Arvidson et al. [88]. During cooling, G' (T) was slightly decreased from 85 to 50 °C followed by a dramatic reduction from 50 to 28 °C owing to the increasing molecular chain mobility. Compared to PH-C, PPH-0 and PPH-8 showed a higher G' (T). This proposes that the high-temperature gelation in these 4D structures was notably higher due

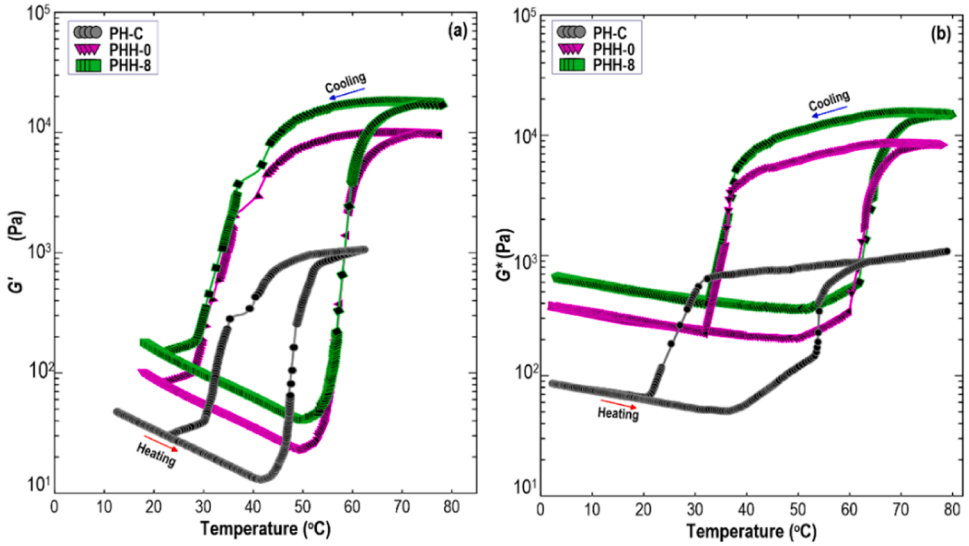

Fig. 10. Thermoreversible behavior of PH-C, PPH-0, and PPH-8. (a) G' and (b) G^* as a function of the heating-cooling process at a heating and cooling rate of 1 °C min^{-1}, 1% strain, and 1 rad s^{-1}.

to the stiff structure of the crosslinked poly-HIPEs. It should be mentioned that the values of G' (T) detected by linear dynamic mechanical spectroscopy (Fig. 10a) were higher than those measured by oscillatory rheological property (Fig. 3). This could be ascribed to the fact that the Pickering-HIPE-based inks were converted to the Poly-Pickering-HIPEs as a function of crosslinking using extrusion-based 3D printing. On the other hand, the complex modulus (G^*) values were increased during the heating process up to 80 °C (Fig. 10b). Upon cooling, there was considerable hysteresis before the 4D printed objects reached a temperature of about 21–30 °C, where the 4D printed structures return to its original state. As reported earlier, a blend of MC and KC possesses a UCST-type transition [88]. Compared to PH-C, the G^* (T) values of PPH-0 and PPH-8 were higher during heating-cooling cycles. This again verifies that the MBA crosslinker during hot-melt

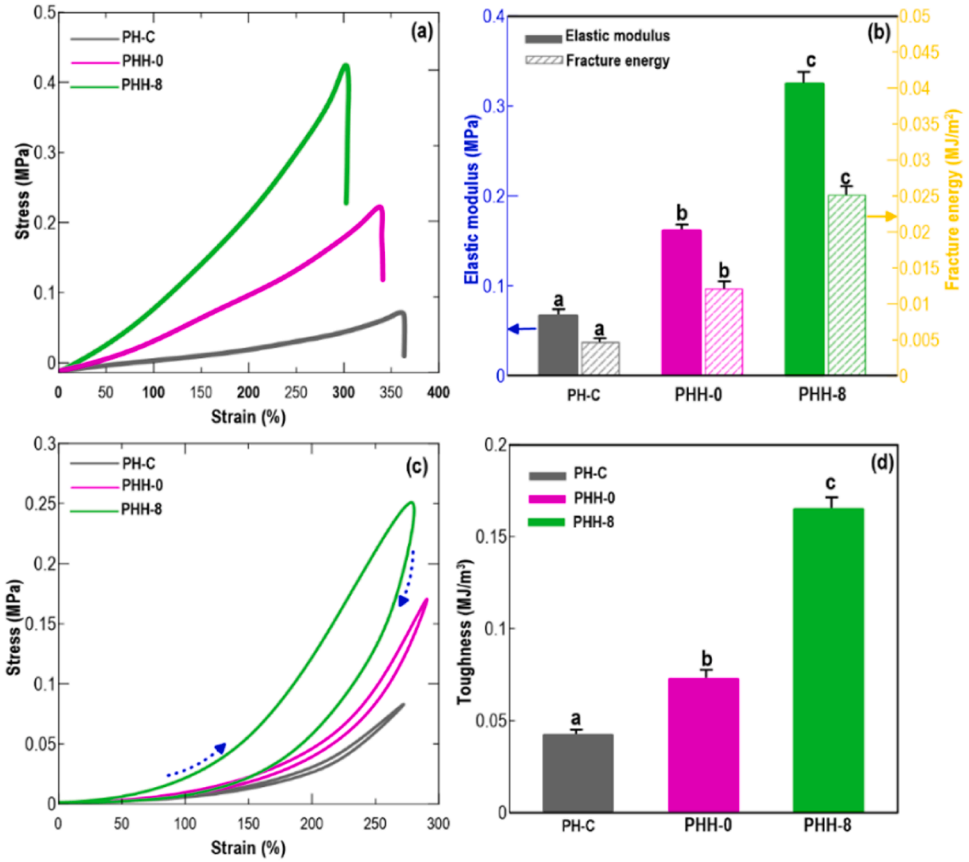

Fig. 11. Mechanical properties of PH-C, PPH-0, and PPH-8. (a) Stress–strain curve. (b) Elastic modulus and fracture energy bar diagrams. (c) Stress–strain curves after unloading–loading test at a 250% strain. (d) toughness values bar diagram.

extrusion-based printing induced some new intramolecular bonds in the 4D printed PPH-0 and PPH-8, which agree well with the previously conducted FT-IR, ^{13}C NMR, contact angel, and AFM measurements. This shows good structural stability of PPH-0 and PPH-8, improving their durability after the printing process. These outcomes justify a brilliant thermoreversible/thermo-responsive behavior with an extraordinary elastic or complex modulus.,

3.2.4. Mechanical strength and self-recovery of 4D printed objects

Fig. 11a,b show a typical tensile stress–strain curve with its relevant stress bar chart for PH-C, PPH-0, and PPH-8 samples. The stress–strain curves obviously showed that the *in-situ* crosslinking during the printing process notably affected the mechanical strength of 4D structures. Compared to PH-C and PPH-0, the PPH-8 showed a higher elastic modulus (*E*) with greater fracture energy (*G*) (Fig. 11a,b). The outstanding mechanical strength of PPH-8 is likely due to an increased crosslinking density of the 4D network owing to the development of intermolecular hydrogen bonds among MC and KC formed during hot-melt 4D printing.

The recoverable properties of 4D structures were further evaluated by a loading–unloading experiment at a 250% strain (Fig. 11c,d). In this case, PH-C showed negligible hysteresis loop and presented small unrecoverable deformation upon the unloading. This offers the presence of a more efficient energy dissipation pathway in its particular network structure. The unrecoverable deformation regarding PPH-0 was also small and remained somewhat unchanged after load–unload cycle (Fig. 11c). This reveals that this 4D structure did not become considerably softened during the loading–unloading process, showing an unrecoverable deformation with low toughness (Fig. 11d). The 4D network structure of PPH-8 object, by contrast, endowed the function of stress transfer and recoverable energy dissipation, thus achieving high toughness and good self-recovery ability [24,34]. The stress–strain curves of different 4D structures during loading–unloading measurements under different strains are also shown in Fig. S-5 (section S.5 in Supplementary Materials). In this case, there was an unimportant hysteresis before 50% strain, and a hysteresis loop emerged after a strain of 50%, which might denote that the 4D printed scaffolds possess two different types of recoverable properties. The 4D objects (especially PPH-8) may offer a characteristic rubber elastic feature concerning low-amplitude deformation, yet they showed good mechanical self-recovery behaviors at the high-amplitude deformation [89,90]. This is possibly elucidated by an interconnected 3D macroporous network in 4D printed structures (as presented in Fig. 6), where hydrogen bonds efficiently develop the stress transfer to the external deformation [24].

4. Conclusion

In conclusion, a 4D printed hierarchical macroporous structure was prepared by *in-situ* crosslinking of the continuous phase of Pickering-HIPE during 3D printing. Before the printing process, the HIPE-based inks containing methylcellulose/kappa-carrageenan were stabilized by a hybrid of cellulose-based nanofibrils and nanocrystals to utilize given phase behaviors in colloidal dispersions *via* depletion effect. The instrumental results showed that the addition of a higher level of cellulose nanofibril into Pickering-HIPEs proved enhanced colloidal stability, improved oscillatory rheological response, and excellent thixotropic behavior. Therefore, a concentration gradient of cellulose nanofibrils existed amongst the aqueous bulk (high cellulose nanofibrils level) and the “depletion zone” that surrounds each droplet (low cellulose nanofibrils level). By converting Pickering-HIPE to poly-Pickering-HIPE, a 4D printed structure with a high level of porosity was fabricated having locally well-behaved consecutive shape alteration upon selective stimuli of heat. The outstanding mechanical strength of 4D printed scaffolds was obtained, which is primarily associated with a reversible fracture of the physical network offering a high level of energy dissipation. The presented approaches and materials compositions signify an important breakthrough for the advanced construction of multi-material 4D printed hierarchical macroporous scaffold. Thus, the proposed practicable technique can be utilized for remotely controllable 4D printing by heat activation, for applications in the fields of soft robotics, biofabrication, and biomedical applications.

Author Contributions

The manuscript was written through the contributions of all authors. All authors have approved the final version of the manuscript.

Funding

The research funding was provided by the University of Natural Resources and Life Sciences Vienna (BOKU).

CRediT authorship contribution statement

Shahbazi Mahdiyar: Writing – original draft, Validation, Supervision, Software, Resources, Methodology, Investigation, Funding acquisition, Formal analysis, Data curation, Conceptualization. **Jäger Henry:** Writing – original draft, Supervision, Funding acquisition, Conceptualization. **Ettelaie Rammile:** Methodology, Investigation, Conceptualization. **Chen Jianshe:** Writing – original draft, Methodology, Data curation. **Mohammadi Adeleh:** Validation, Methodology, Conceptualization. **Asghartabar Kashi Peyman:** Validation, Software, Conceptualization..

Declaration of Competing Interest

The authors declare that they have no known competing financial interests or personal relationships that could have appeared to influence the work reported in this paper.

Data availability

Data will be made available on request.

Appendix A. Supporting information

Supplementary data associated with this article can be found in the online version at doi:10.1016/j.addma.2024.103977.

References

[1] X. Zhang, C. Li, J. Liang, J. Wang, J. Zhang, X.-B. Chen, F. Wang, R. Li, Chemcatchem 12 (2020) 1212.
[2] D. Guan, X. Wang, M. Li, F. Li, L. Zheng, X. Huang, J.-J. Xu, Angew. Chem., Int. Ed. 59 (2020) 19518.
[3] Y.S. Chen, W. Zhang, T. Zhao, F. Li, M. Zhang, J. Li, Y. Zou, W. Wang, S.J. Cobbina, X. Wu, Food Chem. 194 (2016) 712.
[4] L. Wu, C. Zhou, B. Zhang, H. Lei, W. Wang, X.-B. Pu, L. Liu, J. Liang, Y. Fan, X. Zhang, ACS Appl. Mater. Interfaces 12 (2020) 48395.
[5] L. Qin, H. Yi, G. Zeng, C. Lai, D. Huang, P. Xu, Y. Fu, J. He, B. Li, C. Zhang, M. Cheng, H. Wang, C. Lai, J. Hazard. Mater. 380 (2019) 120864.
[6] J. Song, Z. Chen, L.J. Murillo, D. Tang, C. Meng, X. Zhong, T. Wang, J. Li, Int. J. Biol. Macromol. 166 (2021) 1111.
[7] T. Liu, G. Zou, S.-J. Tu, W. Guo, W. Qin, Y. Xie, B. Zhao, L. Zhao, Z. Liang, L. Jiang, ACS Appl. Mater. Interfaces 12 (2020) 28100.
[8] Y.-W. Chen, Y. Shen, C.-C. Ho, J.E. Yu, Y.-H.A. Wu, K. Wang, C.T. Shih, M.-Y. Shie, Mater. Sci. Eng. C. 91 (2018) 679.
[9] J. Jiang, Y. Yuan, H. Wu, X. Li, M. Yuan, W. Huaizhang, X. Wu, S. Liu, X. Zheng, M. Kim, H.-Y. Zheng, S. Rehman, G. Jiang, W. Fu, J. Hazard. Mater. 411 (2021) 125034.
[10] X. Zhao, G. Yu, J. Li, Y. Feng, L. Zhang, Y. Peng, Y.-Y. Tang, L. Wang, ACS Sustain. Chem. Eng. 6 (2018) 4105.
[11] H. Sai, K.W. Tan, K. Hur, E. Asenath-Smith, R. Hovden, Y. Jiang, M.L. Riccio, D. A. Muller, V. Elser, L.A. Estroff, S.M. Gruner, U. Wiesner, Science 341 (2013) 530.
[12] J. Pinto, M. Dumon, M.A. Rodriguez-Perez, R.A. Garcia, C. Dietz, J. Phys. Chem. C. 118 (2014) 4656.
[13] K.C. Krogman, J.L. Lowery, R.D. Reis, G.C. Rutledge, P.T. Hammond, Nat. Mater. 8 (2009) 512.

[14] S.-S. Pan, J. Yin, L. Yu, C. Zhang, Y. Zhu, Y.-S. Gao, Y. Chen, Adv. Sci. 7 (2019) 1901511.
[15] H. Xiang, Q. Yang, Y.-S. Gao, D. Zhu, S.-S. Pan, T. Xu, Y. Chen, Adv. Funct. Mater. 30 (2020) 1909938.
[16] Q. Yang, H. Yin, T. Xu, D. Zhu, J. Yin, Y. Chen, X. Yu, J. Gao, C. Zhang, Y. Chen, Y.-S. Gao, Small 16 (2020) 1906814.
[17] J. Yin, S.-S. Pan, X. Guo, Y.-S. Gao, D. Zhu, Q. Yang, J. Gao, C. Zhang, Y. Chen, Nanomicro Lett. 13 (2021) 1–18.
[18] B. Yang, J. Yin, Y. Chen, S.-S. Pan, H. Yao, Y.-S. Gao, J. Shi, Adv. Mater. 30 (2018) 1705611.
[19] W.-Y. Yan, C. Zhang, L. Liu, ACS Appl. Mater. Interfaces 13 (2021) 45385.
[20] C. Huo, X. Tian, Y. Nan, Q. Zhengping, Q. Zhong, X. Huang, D. Li, *Chem. Eng. J.* 450 (2022) 138259.
[21] B. Stolz, M. Mader, L. Volk, T. Steinberg, R. Mülhaupt, Macromol. Mater. Eng. 306 (2020) 2000541.
[22] Z. Yang, X. Yang, T. Yang, Y. Cao, C. Zhang, Y. Zhang, P. Li, J. Yang, Y. Ma, Q. Li, Energy Stor. Mater. 54 (2023) 51.
[23] M.R. Bidgoli, I. Alemzadeh, E. Tamjid, M. Khafaji, M. Vossoughi, Mater. Sci. Eng. C. 103 (2019) 109688.
[24] M. Shahbazi, H. Jaeger, ACS Appl. Bio Mater. 4 (2020) 325.
[25] M. Shahbazi, H. Jäger, R. Ettelaie, M. Ulbrich, Biomacromolecules 24 (2022) 69.
[26] K. Huang, E. Bernardo, G. Franchin, P. Colombo, Addit. Manuf. 36 (2020) 101549.
[27] Y. Jiang, Z.P. Xu, T. Huang, Y. Liu, F. Guo, C. Gao, W. Gao, Adv. Funct. Mater. 28 (2018) 1707024.
[28] T. Li, D. Zhai, B. Ma, J. Xue, P. Zhao, C. Yang, M. Gelinsky, C. Wu, Adv. Sci. 6 (2019) 1901146.
[29] C. Zhu, G. Liu, F. Qian, T. Han, E.B. Duoss, J.D. Kuntz, C.M. Spadaccini, M. A. Worsley, Y. Li, Nano Lett. 16 (2016) 3448.
[30] B. Coppola, C. Tardivat, S. Richaud, J.M.C. Tulliani, L. Montanaro, P. Palmero, J. Eur. Ceram. Soc. 41 (2021) 3798.
[31] S.S.L. Chan, M.L. Sesso, G.V. Franks, J. Am. Ceram. Soc. 103 (2020) 5554.
[32] Q. Liu, W. Zhai, ACS Appl. Mater. Interfaces 14 (2022) 32196.
[33] M. Shahbazi, H. Jäger, R. Ettelaie, A. Mohammadi, P.A. Kashi, Addit. Manuf. 71 (2023) 103598.
[34] M. Shahbazi, H. Jäger, A. Mohammadi, P.A. Kashi, J. Chen, R. Ettelaie, ACS Appl. Mater. Interfaces 15 (42) (2023) 49874–49891.
[35] S. Liu, M. Jin, Y. Chen, H. Gao, X. Shi, W. Cheng, L. Ren, Y. Wang, J. Mater. Chem. B 5 (2017) 2671.
[36] T. Yang, Y. Hu, C. Wang, B.P. Binks, ACS Appl. Mater. Interfaces 9 (2017) 22950.
[37] D. Nikjoo, F. Akhtar, *J. CO_2 Util.* 21 (2017) 473.
[38] T. Zhang, Q. Guo, J. Chem. Eng. 307 (2017) 812.
[39] T. Zhang, Z. Xu, H. Gui, Q. Guo, J. Mater. Chem. A 5 (2017) 10161.
[40] J. Liu, X. Chen, P. Wang, X. Fu, K. Liu, Y. Fang, Macromol. Rapid Commun. 38 (2017) 1700270.
[41] S. Geng, Y. Li, J. Lv, H. Ma, G. Liang, B. Liu, Food Chem. 373 (2022) 131576.
[42] Y. Hu, S. Zhang, Y. Yang, J. Huang, M. Hu, W. Chen, Z. Tong, C. Wang, ACS Appl. Mater. Interfaces 6 (2014) 17166.
[43] S. Zou, Z. Wei, Y. Hu, Y. Deng, Z. Tong, C. Wang, Polym. Chem. 5 (2014) 4227.
[44] I. Pulko, M. Kolar, P. Krajnc, Sci. Total Environ. 386 (2007) 114.
[45] M. Alikhani, M.R. Moghbeli, J. Chem. Eng. 239 (2014) 93.
[46] Y. Feng, X. Zhang, M. Jin, D. Wan, Part A, J. Polym. Sci. 55 (2016) 1294.
[47] J. Liu, J. Pan, Y. Ma, S. Liu, F. Qiu, Y. Yan, Chem. Eng. J. 332 (2018) 517.
[48] S. Kovačič, M. Silverstein, Macromol. Rapid Commun. 37 (2016) 1814.
[49] N.R. Cameron, Polymer 46 (2005) 1439.
[50] (a) Y. Yang, Z. Wei, C. Wang, Z. Tong, Chem. Comm. 49 (2013) 7144; (b) M. Qiao, X. Yang, Y. Zhu, G. Guerin, S. Zhang, Langmuir 36 (23) (2020) 6421–6428.
[51] B.P. Binks, Curr. Opin. Colloid Interface 7 (2002) 21.
[52] P.J. Colver, S.A.F. Bon, Chem. Mater. 19 (2007) 1537.
[53] P. Viswanathan, S. Chirasatitsin, K. Ngamkham, A.J. Engler, G. Battaglia, J. Am. Chem. Soc. 134 (2012) 20103.
[54] K. Haibach, A. Menner, R.R. Powell, A. Bismarck, Polymer 47 (2006) 4513.
[55] Z. Zheng, X.-H. Zheng, H. Wang, Q. Du, ACS Appl. Mater. Interfaces 5 (2013) 7974.
[56] A. Vílchez, C. Rodríguez-Abreu, J. Esquena, A. Menner, A. Bismarck, Langmuir 27 (2011) 13342.
[57] I. Capron, B. Cathala, Biomacromolecules 14 (2013) 291.
[58] C.E. Salas, H. Sixta, C. Rodríguez-Abreu, C. Carrillo, O.J. Rojas, Curr. Opin. Colloid Interface 19 (2014) 383.
[59] H.H. Mert, M.R. Moghbeli, S. Sajad, E.H. Mert, React. Funct. Polym. 151 (2020) 104572.
[60] L. Bai, S. Huan, W. Xiang, O.J. Rojas, Green. Chem. 20 (2018) 1571.
[61] Y. Nahar, P. Wei, C. Cipriani, A. Khodabandeh, A.C. Bissember, E. Pentzer, S. C. Thickett, ACS Appl. Mater. Interfaces 4 (2022) 8429.
[62] H. Xu, X.-H. Zheng, Y. Huang, H. Wang, Q. Du, Langmuir 32 (2015) 38.
[63] Z. Liu, P. Yao, Carbohydr. Polym. 132 (2015) 490.
[64] A.R. Patel, E.M. Drost, R.D. Adel, J. Hazekamp, A. Imhof, Soft Matter 8 (2012) 3515.
[65] N. Contessi, L. Altomare, A. Filipponi, S. Farè, Mater. Lett. 207 (2017) 157–160.
[66] A.K. Sharma, A. Gupta, A. Dhiman, M. Garg, R. Mishra, G. Agrawal, Colloids Surf. A: Physicochem. Eng. Asp. 654 (2022) 130155.
[67] M. Tomšič, F. Prossnigg, O. Glatter, J. Colloid Interface Sci. 322 (2008) 41.
[68] A.M. Atta, H.S. Ismail, A.M. Elsaaed, J. Appl. Polym. Sci. 123 (4) (2012) 2500–2510.
[69] G. Jiang, Z. Deng, Y. He, Z. Li, X. Ni, *J. Pet. Sci. Eng.* 181 (2019) 106250.
[70] A. Pajouhandeh, A. Kavousi, M. Schaffie, M. Ranjbar, Colloids Surf. A: Physicochem. Eng. Asp. 520 (2017) 597.
[71] O. Mengual, G. Meunier, I. Cayré, K. Puech, P. Snabre, Talanta 50 (1999) 445.
[72] Z. Li, H. Wu, M. Yang, J. Jiang, D. Xu, H. Feng, Y. Lu, W. Kang, B. Bai, J. Hou, Energ. Fuel. 32 (2018) 3119.
[73] T. Hoare, E.D. Cranston, Chem. Mater. 29 (2017) 4609.
[74] M. Shahbazi, H. Jäger, R. Ettelaie, Colloids Surf. A: Physicochem. Eng. 622 (2021) 126641.
[75] M. Shahbazi, H. Jäger, R. Ettelaie, J. Chen, Food Hydrocoll. 120 (2021) 106967.
[76] M. Shahbazi, H. Jäger, R. Ettelaie, ACS Appl. Mater. Interfaces 14 (2022) 21392.
[77] M. Shahbazi, H. Jäger, R. Ettelaie, J. Agric. Food Chem. 70 (2022) 2374.
[78] M. Gestranius, P. Stenius, E. Kontturi, J. Sjöblom, T. Tammelin, Colloids Surf. A: Physicochem. Eng. Asp. 519 (2017) 60.
[79] A.R. Osi, H. Zhang, J.M. Chen, Y. Zhou, R. Wang, J. Fu, P. Müller-Buschbaum, Q. Zhong, ACS Appl. Mater. Interfaces 13 (2021) 22902.
[80] H. Geng, Carbohydr Polym 186 (2018) 208–216.
[81] A. Mohammadi, P.A. Kashi, M. Kashiri, A. Bagheri, J. Chen, R. Ettelaie, H. Jäger, M. Shahbazi, Food Hydrocollo 142 (2023) 108851.
[82] M. Glumac, C. Ritzoulis, J. Chen, Food Hydrocoll. 97 (2019) 105195.
[83] Q. Chen, S. Xu, Q. Liu, J.H. Masliyah, Z. Xu, Adv. Colloid Interface Sci. 233 (2016) 94.
[84] Z. Yang, L. Wang, Q. Sun, D.J. McClements, X. Xu, Food Hydrocoll. 128 (2022) 107560.
[85] M. Tomsic, S.G. uillot, L. Sagalowicz, M.E. Leser, O. Glatter, Langmuir 25 (16) (2009) 9525–9534.
[86] J. Zhou, C. Chang, R. Zhang, L. Zhang, Macromol. Biosci. 7 (6) (2007) 804–809.
[87] M.R. Mangione, D. Giacomazza, D. Bulone, V. Martorana, P.L. San Biagio, Biophys. Chem. 104 (1) (2003) 95–105.
[88] S.A. Arvidson, J.R. Lott, J.W. McAllister, J. Zhang, F.S. Bates, T.P. Lodge, M. Brackhagen, Macromolecules 46 (1) (2013) 300–309.
[89] M. Shahbazi, H. Jäger, S.J. Ahmadi, M. Lacroix, Carbohydr. Polym. 240 (2020) 116211.
[90] M. Shahbazi, H. Jäger, R. Ettelaie, Biomacromolecules 22 (11) (2021) 4592–4605.